The Astrophysical Journal, 713:356–373, 2010 April 10 doi:10.1088/0004-637X/713/1/356

FORMATION AND EVOLUTION OF DUST IN TYPE IIb SUPERNOVAE WITH APPLICATION TO THE CASSIOPEIA A SUPERNOVA REMNANT

Takaya Nozawa[1], Takashi Kozasa[2], Nozomu Tominaga[1,3], Keiichi Maeda[1], Hideyuki Umeda[4], Ken'ichi Nomoto[1,4], and Oliver Krause[5]
[1] Institute for the Physics and Mathematics of the Universe, University of Tokyo, Kashiwa, Chiba 277-8583, Japan; tnozawa@mail.sci.hokudai.ac.jp
[2] Department of Cosmosciences, Graduate School of Science, Hokkaido University, Sapporo 060-0810, Japan
[3] Department of Physics, Faculty of Science and Engineering, Konan University, Okamoto, Kobe 658-8501, Japan
[4] Department of Astronomy, School of Science, University of Tokyo, Bunkyo-ku, Tokyo 113-0033, Japan
[5] Max-Planck-Institut für Astronomie, Königstuhl 17, 69117 Heidelberg, Germany
Received 2009 September 21; accepted 2010 February 23; published 2010 March 22

ABSTRACT

The amount and size of dust formed in the ejecta of core-collapse supernovae (CCSNe) and injected into the interstellar medium (ISM) depend on the type of CCSNe through the varying thicknesses of their outer envelopes. Recently Cas A was identified as a Type IIb SN (SN IIb) that is characterized by a small-mass hydrogen envelope. In order to clarify how the amount of dust formed in the ejecta and supplied into the ISM depends on the type of CCSNe, we investigate the formation of dust grains in the ejecta of an SN IIb and their evolution in the shocked gas in the SN remnant (SNR) by considering two sets of density structures (uniform and power-law profiles) for the circumstellar medium (CSM). Based on these calculations, we also simulate the time evolution of thermal emission from the shock-heated dust in the SNR and compare the results with the observations of Cas A SNR. We find that the total mass of dust formed in the ejecta of an SN IIb is as large as 0.167 $M_\odot$ but the average radius of dust is smaller than 0.01 μm and is significantly different from those in SNe II-P with massive hydrogen envelopes; in the explosion with the small-mass hydrogen envelope, the expanding He core undergoes little deceleration, so that the gas density in the He core is too low for large-sized grains to form. In addition, the low-mass hydrogen envelope of the SN IIb leads to the early arrival of the reverse shock at the dust-forming region. If the CSM is more or less spherical, then the newly formed small grains would be completely destroyed in the relatively dense shocked gas for the CSM hydrogen density of $n_{\rm H} > 0.1$ cm^{-3} without being injected into the ISM. However, the actual CSM is likely to be non-spherical, so a portion of the dust grains could be ejected into the ISM without being shocked. We demonstrate that the temporal evolution of the spectral energy distribution (SED) by thermal emission from dust is sensitive to the ambient gas density and structure that affects the passage of the reverse shock into the ejecta. Thus, the SED evolution reflects the evolution of dust through erosion by sputtering and stochastic heating. For Cas A, we consider the CSM produced by the steady mass loss of $\dot{M} \simeq 8 \times 10^{-5}\ M_\odot$ yr^{-1} during the supergiant phase. Then we find that the observed infrared SED of Cas A is reasonably reproduced by thermal emission from the newly formed dust of 0.08 $M_\odot$, which consists of the 0.008 $M_\odot$ shock-heated warm dust and 0.072 $M_\odot$ unshocked cold dust.

Key words: dust, extinction – infrared: ISM – ISM: supernova remnants – shock waves – supernovae: general – supernovae: individual (Cassiopeia A)

Online-only material: color figures

1. INTRODUCTION

Core-collapse supernovae (CCSNe) are considered to be important sources of interstellar dust. They eject a large amount of heavy elements synthesized during their stellar evolution and explosive burning, and form dust grains inside the dense, metal-rich He core in the expanding ejecta. Meanwhile, the reverse and forward shocks driven by the encounter of the ejecta materials with the surrounding medium propagate into the supernova (SN) ejecta and the interstellar medium (ISM), respectively, producing the hot gas plasma within the supernova remnant (SNR). The dust grains formed in the He core, before being dispersed into interstellar space, pass through the shock-heated gas and suffer from erosion and destruction by sputtering due to collisions with the energetic ions. Since the efficiency of destruction of dust grains depends heavily on their composition and size, the composition and size of dust that condenses in the ejecta should be clarified for understanding the properties and amount of dust finally injected from CCSNe into the ISM.

Observations of nearby CCSNe have reported increasing evidence for dust formation in the ejecta (see Kozasa et al. 2009, for review). Nevertheless, the composition and size of newly formed dust have not been specified except in two cases: SN 2004et (Kotak et al. 2009) and SN 2006jc (Sakon et al. 2009; Smith et al. 2008; Mattila et al. 2008). The masses of dust formed in the SN ejecta are estimated to be less than $10^{-3}\ M_\odot$ from the observations by assuming usually that the ejecta is optically thin for thermal emission of dust. However, newly formed dust may reside in optically thick clumps (e.g., Meikle et al. 2007). Moreover, some species of dust grains can cool down quickly after the formation (Nozawa et al. 2008), so that near- to mid-infrared (IR) observations could miss the cold dust. Hence, the derived mass of dust could be the lower limit in some cases, and sophisticated radiative transfer calculations (e.g., Sugerman et al. 2006; Ercolano et al. 2007) referring to the observational data at UV/optical to far-IR wavelengths would be required to deduce the properties and mass of dust formed in the ejecta from observations.

Theoretical studies have shown that various species of dust grains with a radius of 0.001–1 μm and a total mass of 0.1–1 $M_\odot$ can condense in the ejecta of Type II-P SNe (SNe II-P) retaining a massive hydrogen envelope (Kozasa et al. 1989, 1991; Todini & Ferrara 2001; Nozawa et al. 2003). Adopting the results of dust formation calculations, a semi-analytical model (Bianchi & Schneider 2007) and a numerical simulation (Nozawa et al. 2007) investigated the survival of dust in the SNRs and found that the dust mass injected into the uniform ISM is $\sim$0.01–0.8 $M_\odot$ for the ambient hydrogen density of $n_{\rm H,0}$ = 10–0.1 cm^{-3}. This mass of dust supplied by SNe II-P is still large enough to explain a huge quantity of dust in excess of 10^8 $M_\odot$ observed for the host galaxies of quasars at redshift $z > 5$ (Morgan & Edmunds 2003; Maiolino et al. 2006; Dwek et al. 2007), though it is proposed that asymptotic giant branch stars can also contribute to dust enrichment even at such an early epoch (Valiante et al. 2009).

Recently Kozasa et al. (2009) have suggested that the amount and size of dust formed in the ejecta and injected into the ISM depend on the type of CCSNe, reflecting the thickness of the H-rich envelope. A less massive outer envelope leads to extremely high expansion velocity of the He core unless the kinetic energy of the explosion is very low, and makes the gas density in the expanding ejecta of the He core too low for large-sized grains to be produced. Furthermore, a low-mass outer envelope can allow the reverse shock to arrive early at the dust-forming region and result in efficient destruction of newly formed dust in the shock-heated gas with high density. Because a significant fraction of CCSNe ($\sim$0.3) explode as hydrogen/helium-poor CCSNe such as SNe Ib/Ic and SNe IIb (Prieto et al. 2008; Smartt et al. 2009; Boissier & Prantzos 2009), it is essential to investigate how the formation and destruction processes of dust depend on the type of CCSNe, in order to clarify the role of CCSNe as sources of interstellar dust.

It should be mentioned here that dust grains embedded in the postshock gas are eroded by sputtering and are heated up by collisions with the hot gas, radiating their thermal emission at IR wavelengths. Since the destruction efficiency and the heating rate of dust are sensitive to grain size as well as gas density, the IR spectral energy distributions (SEDs) by thermal emission from dust in SNRs can be a diagnostic feature of the size and temperature of dust, and therefore provide key information on the nature of dust formed in the ejecta, density structure in the ambient medium, and destruction and heating processes of dust. In particular, young SNRs that originated from SNe with low-mass envelopes are ideal for comparing the observed IR SEDs with calculated ones; the reverse shock can quickly arrive at the He core and heat up newly formed dust before the forward shock sweeps up a considerable amount of circumstellar/interstellar dust, so that we mainly see the IR emission from dust grains condensed in the ejecta. Cassiopeia A (Cas A) SNR is one of the best targets for this study because the Cas A SN has been recently identified as Type IIb by a striking similarity between the optical spectrum of its scattered light echo and the time-averaged spectrum of SN IIb 1993J (Krause et al. 2008), and the presence of dust freshly formed in the ejecta has been confirmed by IR observations (e.g., Rho et al. 2008).

In this paper, we explore the formation of dust in an SN IIb and the evolution of the dust inside the SNR, with the aim of revealing the composition, size, and mass of dust ejected from hydrogen-deficient CCSNe. In addition, the time evolution of thermal emission from dust within SNRs is calculated and is compared with observations of Cas A to discuss the composition and amount of dust. In Section 2, we perform a calculation of dust formation in the ejecta of an SN IIb whose progenitor has lost most of its hydrogen envelope during the evolution (Nomoto et al. 1993; Podsiadlowski et al. 1993). In Section 3, we investigate the evolution of the newly formed dust in the gas heated by the reverse and forward shocks and its dependence on the ambient gas density and structure. Then, following the calculations of dust evolution in SNRs, we present the temporal evolution of IR emission from collisionally heated dust in the hot gas in Section 4, and compare the results with observations of Cas A in Section 5. We summarize our results in Section 6.

2. FORMATION OF DUST IN THE EJECTA OF SN IIb

In the ejecta of SNe, dust formation takes place within the He core where the densities of condensible elements are high enough to advance the formation and growth of seed nuclei through collisions with the relevant gas species. Formation processes of dust grains are influenced by the time evolution of the density and temperature of the gas as well as the elemental composition in the ejecta (Kozasa et al. 1989). In this section, we describe a model of the dust formation calculation for an SN IIb and present the results of the calculations.

2.1. Model of SN IIb and Calculation of Dust Formation

The calculation of dust formation is carried out by applying the theory of non-steady state nucleation and grain growth developed by Nozawa et al. (2003). The theory takes into account chemical reactions at condensation, considering that the kinetics of nucleation and grain growth is controlled by the key species defined as the gas species with the least collisional frequency among the reactants (Kozasa & Hasegawa 1987; Hasegawa & Kozasa 1988). Given the elemental composition of the gas in the ejecta as well as the time evolution of the gas density and temperature, the theory allows us to determine the condensation time, chemical composition, size distribution, and mass of dust that condenses in the ejecta (see Nozawa et al. 2003 for details).

In the calculation of dust formation, we adopt the model of the SN IIb with a zero-age main-sequence mass of 18 $M_\odot$ and a metallicity of $Z = 0.02$. The ejecta mass is $M_{\rm eje} = 2.94$ $M_\odot$, the mass of the hydrogen envelope is $M_{\rm env} = 0.08$ $M_\odot$, the kinetic energy of the explosion is $E_{\rm kin} = 10^{51}$ erg, and the synthesized ^{56}Ni mass is $M(^{56}{\rm Ni}) = 0.07$ $M_\odot$. These model parameters are invoked to reproduce the light curve of SN 1993J by referring to the SN model in Shigeyama et al. (1994). Note that the mass of ejecta in this model is in good agreement with the ejecta mass of Cas A (=2–4 $M_\odot$) estimated from the studies of shock dynamics (Borkowski et al. 1996; Chevalier & Oishi 2003; Laming & Hwang 2003) and from X-ray observations (Vink et al. 1996; Favata et al. 1997; Willingale et al. 2003).

In Figure 1, we show the elemental composition in the ejecta of the SN IIb model at 600 days after the explosion, taking into account the decay of radioactive elements. In Table 1, we also present the mass of the dust-forming elements i in the ejecta. We assume that the elemental distribution in the ejecta remains an onion-like structure without any mixing, which is consistent with the theoretical model of mixing in SN 1993J; Iwamoto et al. (1997) have shown with a two-dimensional simulation that the deceleration of the He core by the thin H-rich envelope is so weak that the growth of the Rayleigh–Taylor instability is too slow to cause substantial mixing in the ejecta, in contrast to SN 1987A which has a thick

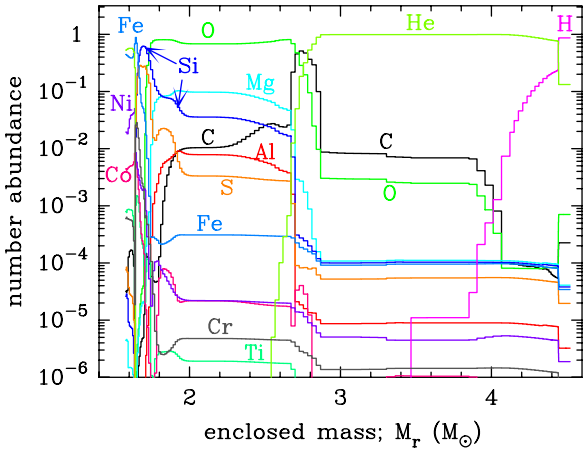

Figure 1. Relative number abundance of elements in the ejecta of the SN IIb model at 600 days after the explosion as a function of enclosed mass. The decay of radioactive elements is taken into account, and the original onion-like structure is assumed to be preserved without any mixing of elements. The progenitor mass of the SN IIb is 18 $M_\odot$, and the mass at the explosion is 4.52 $M_\odot$. The mass cut is 1.58 $M_\odot$, which results in the ejecta mass of 2.94 $M_\odot$. The mass of the hydrogen envelope is 0.08 $M_\odot$.

H-rich envelope (e.g., Hachisu et al. 1990, 1992). Although the jet formation in the explosion suggested from the observations of Cas A can lead to macroscopic mixing (e.g., Tominaga 2009), a simple argument of molecular diffusion has shown that mixing at the atomic level is extremely ineffective before the condensation of dust grains in the ejecta (Deneault et al. 2003). Indeed, the observations of Cas A at various wavelengths have suggested that the mixing in the ejecta should not be at atomic level but at the macroscopic level (e.g., Willingale et al. 2002; Fesen et al. 2006b; Ennis et al. 2006). From Figure 1, we can see the layered structure of elemental composition with the very thin hydrogen envelope at the outermost ejecta, which is followed by the C-rich (C/O > 1) He layer, the O-rich layer, the Si–S–Fe layer, and the Fe–Ni layer inwardly.

The distributions of gas temperature and density in the ejecta of the SN IIb at 300 days and 600 days are shown in Figures 2(a) and (b), compared with those for the SN II-P model of $M_{\rm eje} = 17\,M_\odot$ and $M_{\rm env} = 13.2\,M_\odot$ with the same $E_{\rm kin}$ and $M(^{56}{\rm Ni})$ as those of the SN IIb model (Umeda & Nomoto 2002). The gas density scales as t^{-3} with the time t after the explosion, and the time evolution of the gas temperature is mainly regulated by the energy deposited from radioactive elements (i.e., $M(^{56}{\rm Ni})$). It should be noted that the gas density in the He core of the SN IIb is about three orders of magnitude lower than that in the SN II-P. The reason for this is that, since almost all of the explosion energy is deposited into the He core without the thick hydrogen envelope, the resulting expansion velocity of the gas in the He core of the SN IIb is much higher than that of the SN II-P, as shown in Figure 2(c).

Based on the hydrodynamic and nucleosynthesis models for the SN IIb, we calculate dust formation. Dust formation proceeds through the formation and growth of seed nuclei as the gas cools down. The number of seed nuclei is evaluated by calculating the non-steady state nucleation rate (Equation (5) in Nozawa et al. 2003) coupled with the time evolution of the gas temperature and the number density of the key species. In the calculations, it is assumed that without coagulation the seed nuclei grow homogeneously at a rate controlled by the collisions of the key species with the sticking probability of unity. We also assume that the formation of CO and SiO molecules is complete;

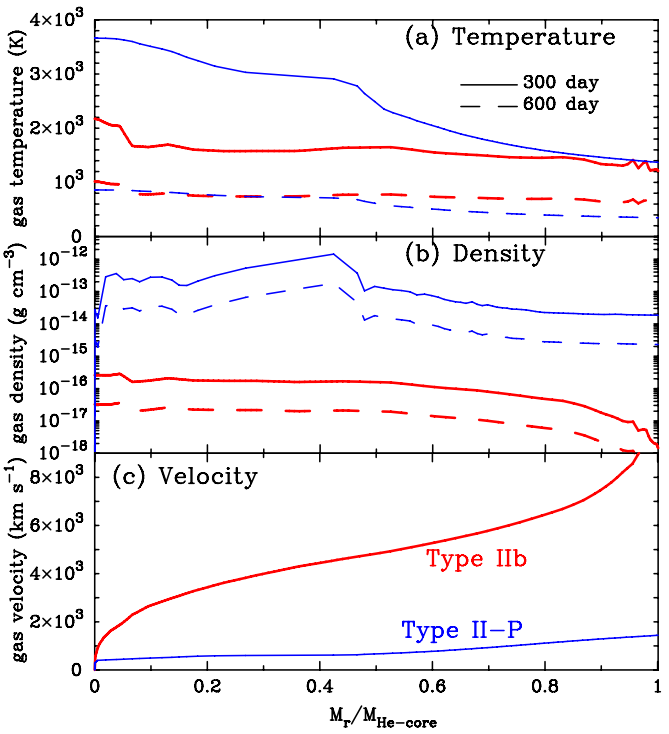

Figure 2. Structures of (a) temperature and (b) density of the gas within the He core at day 300 (solid lines) and day 600 (dashed lines) after the explosion, and (c) the velocity distribution for the SN IIb model (thick lines). For comparison, those for the SN II-P model (thin lines) with $M_{\rm eje} = 17\,M_\odot$ and $M_{\rm env} = 13.2\,M_\odot$ (Umeda & Nomoto 2002) are also shown. The mass coordinate is normalized by the mass of the He core. Note that both SN models have $E_{\rm kin} = 10^{51}$ erg and $M(^{56}{\rm Ni}) = 0.07\,M_\odot$.

all C (Si) atoms are locked in CO (SiO) molecules in the case where the number density of C (Si) atoms is lower than that of O atoms. Under this assumption, C-bearing grains can condense only in the He layer with C/O > 1. Depletion or rarefaction of the key species due to grain growth or the expansion of the ejecta, respectively, causes the process of nucleation and growth of dust grains to cease in less than a few tens of days from the onset of nucleation.

2.2. Results of Dust Formation Calculation

The simulation results of dust formation in SN IIb are illustrated in Figures 3(a) and (b), where the mass distribution and average radius of each dust species formed in the ejecta are given as a function of enclosed mass M_r, respectively. Without any mixing of elements, different species of dust condense according to the elemental composition of the gas in each layer: C grains in the He layer, silicates ($MgSiO_3$, Mg_2SiO_4, and SiO_2) and oxides (Al_2O_3 and MgO) in the O-rich layer, and FeS and Si grains in the Si–S–Fe layer. The typical times (gas temperatures) at which dust grains condense in the ejecta are 300–350 days (1400–1700 K) for C grains, 350–500 days (1100–1400 K) for silicate and oxide grains, and 600–700 days (800–900 K) for Si and FeS grains. In the innermost Fe–Ni layer, neither Fe nor Ni grains can be formed because the gas density becomes too low before the gas cools down to the temperatures ($\lesssim$800 K) at which these grains can condense. Fe atoms residing in both the O-rich and He layers are not abundant enough to be locked in grains as Fe-bearing dust (see Figure 1). Except for Fe grains, the major species of dust formed in the SN IIb are the same as those for the unmixed cases in SNe II-P with $Z = 0$ in Nozawa et al. (2003).

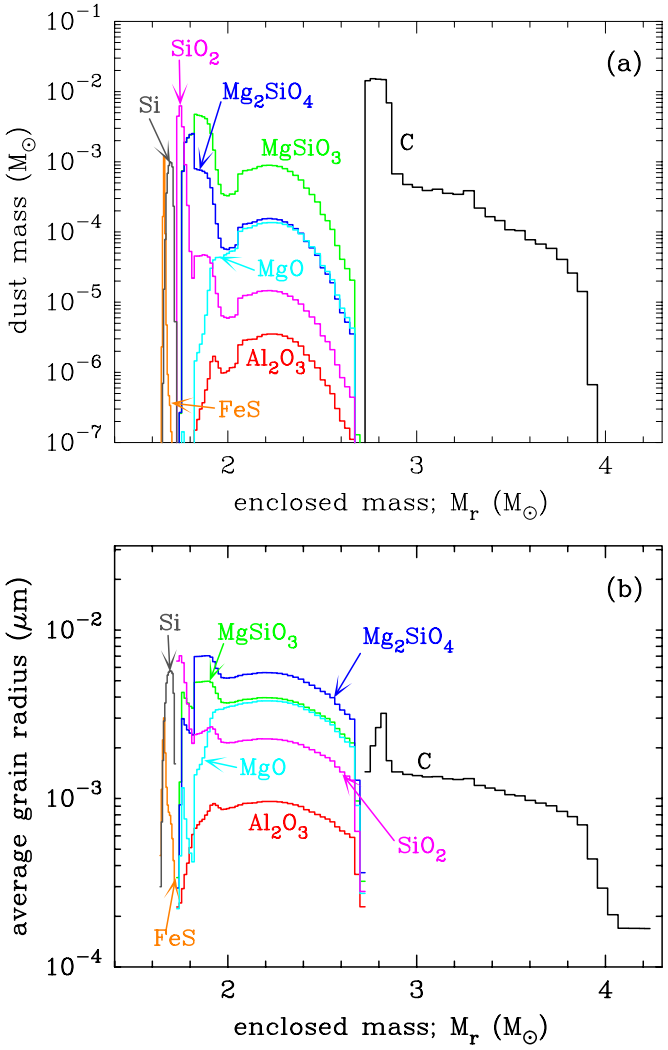

Figure 3. (a) Mass distribution and (b) average radius of each dust species formed in the ejecta of the SN IIb model as a function of enclosed mass.

The mass of each dust species formed in the ejecta of SN IIb is presented in Table 2, together with the ratio of its mass to the total dust mass (see Table 1 for the mass and mass fraction of major elements locked in dust grains). The total mass of newly formed dust is 0.167 $M_\odot$, which is more than two orders of magnitude larger than the dust mass estimated from a handful of observations of nearby dust-forming SNe. C grains are the most dominant species in mass, with the mass of 0.07 $M_\odot$, and the bulk of them is in the innermost He layer at $M_r = 2.7$–$2.9\,M_\odot$ (see Figure 3(a)), where the mass fraction of available C atoms locked in C grains is $f_C = 0.4$–1. The masses of $MgSiO_3$, Mg_2SiO_4, and SiO_2 are 0.055 $M_\odot$, 0.017 $M_\odot$, and 0.016 $M_\odot$, respectively, and these silicate grains account for more than 50% of the total dust mass. The mass distributions of silicate grains are influenced by the abundance of SiO molecules (namely Si atoms, see Figure 1), and concentrate at $M_r = 1.7$–$1.9\,M_\odot$ with the mass fraction of the preexisting SiO molecules locked in silicate grains $f_{Si} = 0.4$–0.8. The condensation efficiency, defined as the ratio of the total dust mass to the total metal mass, is $\simeq$0.13 for the SN IIb and lies in the range of those estimated for SNe II-P (0.05–0.25; Nozawa et al. 2003).

It should be emphasized here that, as can be seen from Figure 3(b), the average radii of all grain species formed in the SN IIb are below 0.01 μm and are much smaller than those

Table 1
Mass of the Main Refractory Species in the Ejecta of the SN IIb

Species (1)	$M_{A,i}$ ($M_\odot$) (2)	$M_{A,i}^{\rm dust}$ ($M_\odot$) (3)	$M_{A,i}^{\rm dust}/M_{A,i}$ (4)
C	1.14×10^{-1}	7.08×10^{-2}	0.621
O	6.86×10^{-1}	4.35×10^{-2}	0.063
Mg	1.07×10^{-1}	2.05×10^{-2}	0.192
Al	9.31×10^{-3}	3.28×10^{-5}	0.004
Si	1.07×10^{-1}	3.12×10^{-2}	0.292
S	3.33×10^{-2}	5.35×10^{-4}	0.016
Fe	7.92×10^{-2}	9.35×10^{-4}	0.012
Others	1.61×10^{-1}	0	0
Total	1.30	0.167	...

Notes. Column 1: species of the main heavy element in the ejecta of the SN IIb. Column 2: mass of each heavy element ($M_{A,i}$). Column 3: mass of each element that is locked up in dust grains at the time of dust formation ($M_{A,i}^{\rm dust}$). Column 4: mass fraction of each element that is locked up in dust grains at the time of dust formation ($M_{A,i}^{\rm dust}/M_{A,i}$).

Table 2
Mass of Each Dust Species Formed in the Ejecta of the SN IIb

Dust Species (1)	$M_{d,j}$ ($M_\odot$) (2)	$M_{d,j}/M_d$ (3)	$M_{d,j}/M_A$ (4)
C	7.08×10^{-2}	0.423	0.054
Al_2O_3	6.19×10^{-5}	3.7×10^{-4}	4.8×10^{-4}
$MgSiO_3$	5.46×10^{-2}	0.326	0.042
Mg_2SiO_4	1.74×10^{-2}	0.104	0.013
SiO_2	1.57×10^{-2}	0.094	0.012
MgO	2.36×10^{-3}	0.014	1.8×10^{-3}
FeS	1.47×10^{-3}	0.009	1.1×10^{-3}
Si	5.07×10^{-3}	0.030	3.9×10^{-3}
Total	0.167	1	0.128

Notes. Column 1: species of dust formed in the ejecta of the SN IIb. Column 2: mass of each grain species ($M_{d,j}$). Column 3: ratio of mass of each dust species to the total dust mass ($M_{d,j}/M_d$). Column 4: ratio of mass of each dust species to the total metal mass ($M_{d,j}/M_A$).

($a_{\rm ave} > 0.01\,\mu$m) of dust grains formed in SNe II-P (Nozawa et al. 2003). This difference is caused by the difference in the gas density within the expanding ejecta of the He core. In general, a larger supercooling necessary for dust grains to condense in a gas with lower density leads to the formation of a large number of seed nuclei and results in smaller average radii even if all available gaseous atoms are used up for the growth of seed nuclei ($f_j = 1$, where f_j is the mass fraction of key species j locked in a given grain species). As was discussed in Kozasa et al. (1989), under the condition that the number density of key species is so low that the collision timescale of key species is longer than the expansion timescale of the gas, neither a significant number of seed nuclei can condense nor nucleated grains can grow to sufficiently large radii via accretion onto the surface of the grains.

2.3. Dependence of Grain Radius on SN Parameters

Here we briefly discuss how our results on dust formation are affected by the model parameters for an SN explosion, in particular focusing on the kinetic energy of the explosion $E_{\rm kin}$. A lower $E_{\rm kin}$ leads to a higher He core density, thus making it possible for more dust grains with larger radii to condense if the time evolution of the gas temperature could not be affected by the explosion energy. At a fixed time t_1, the gas density is scaled by the expansion velocity $v_{\rm eje}$ as $\rho_{\rm eje}(t_1) \propto v_{\rm eje}^{-3}$

for a given mass and density structure of the ejecta. Since $v_{\rm eje} \propto (E_{\rm kin}/M_{\rm eje})^{1/2}$ and roughly $a_{\rm ave} \propto \rho_{\rm eje}^{1/3}$ (Nozawa et al. 2003), we find $a_{\rm ave} \propto 1/v_{\rm eje} \propto (M_{\rm eje}/E_{\rm kin})^{1/2}$. Thus, even for the extremely low explosion energy of $E_{\rm kin} = 10^{50}$ erg, the increase in the average grain radii is as small as a factor of $\simeq 3$. In addition, if we consider $E_{\rm kin} = (1\text{–}4)\times 10^{51}$ erg estimated for Cas A (Willingale et al. 2003; Chevalier & Oishi 2003; Laming & Hwang 2003; Young et al. 2006), grain radii only reduce by a factor of $\lesssim 2$, compared with those given in Figure 3(b).

In reality, however, the assessed variation of the grain radius is suppressed by the dependence of the time evolution of gas temperature on $E_{\rm kin}$; with the same amount of ^{56}Ni in the ejecta, the lower (higher) explosion energy can cause the gas temperature to decrease more slowly (more quickly) because of more (less) efficient energy deposition in the ejecta with the higher (lower) gas density. This leads to the later (earlier) condensation of dust, which compensates for the increase (decrease) in the gas density. Consequently, the condensation of dust occurs at a similar gas density, and not only the radius but also the mass of dust formed in the ejecta is almost the same, regardless of the explosion energy (see Appendix A in Nozawa et al. 2003), as long as the range of variation of $E_{\rm kin}$ is not extremely large. The qualitative analysis indicates that the grain radius is insensitive to the explosion energy, and that our results on dust formation are robust for the expected variation of model parameters for Cas A SN.

On the other hand, it should be noted that the grain radius is greatly affected by the structure of the progenitor star resulting from the presence or absence of a massive outer envelope; as seen from Figure 2(c), the He-core velocity of the SN IIb with the thin hydrogen envelope is 5–10 times higher than that of the SN II-P with the thick envelope. The higher velocity of the SN IIb leads to a few orders of magnitude lower gas density and thus produces about one order of magnitude smaller dust grains than the SN II-P. Nozawa et al. (2008) have also pointed out the effect of the lack of the outer envelope on the size of newly formed dust in Type Ib SN 2006jc, applying the SN model by Tominaga et al. (2008). They found that too low gas density in the He core, which is caused by the absence of the outer envelope, prevents dust grains with radii larger than 0.01 μm from forming within the He core. These results indicate that the radii of dust grains formed in SNe IIb and SNe Ib/Ic are generally smaller than those in SNe II-P with thick outer envelopes.

Our results demonstrate that the composition and mass of dust grains formed in the ejecta are almost independent of the type of CCSNe and the initial metallicity of the progenitors because the distribution and yield of metals in the He core are similar. On the other hand, their radii strongly depend on the type of CCSNe; SNe with lower-mass envelopes produce much smaller dust grains ($a_{\rm ave} < 0.01\,\mu$m) than SNe II-P with much more massive envelopes. As shown in the next section, the small sizes of newly formed dust grains will determine their subsequent fates within the SNR.

3. EVOLUTION OF DUST IN TYPE IIb SNR

Dust grains formed in the He core initially move with the gas without suffering from any processings. Upon encountering the reverse shock, the gas is quickly decelerated, while the dust grains decouple from the gas with high velocities relative to the gas, and intrude into the hot plasma region created by the passage of the reverse and forward shocks. These shocked dust grains are decelerated by the drag force, eroded by thermal and/or kinetic sputtering, and heated up by collisions with the hot gas. The motion, destruction, and heating of dust depend not only on the properties of dust but also on the density and temperature in the postshock gas. In this section, applying the result of the dust formation calculation, we examine the evolution of the dust in the hot gas within SNRs and its dependence on the gas density and structure in the circumstellar medium (CSM).

3.1. Model of Calculations for Destruction and Motion of Dust in SNRs

The calculations of dust evolution within SNRs follow the method described by Nozawa et al. (2007); dust grains are treated as test particles, and the motion and destruction of dust are pursued by self-consistently calculating the erosion due to sputtering and the deceleration caused by the gas drag together with the time evolution of gas temperature and density in the spherical symmetry shock. We use the size distribution and spatial distribution of each dust species obtained in the last section as the initial conditions, and adopt the model of the SN IIb used in Section 2 for the velocity and density structure in the ejecta.

For the structure of CSM, which affects the evolution of SNRs and thus critically impacts the evolution of dust, we consider two sets of the density profile. One is the uniform CSM with the hydrogen number densities of $n_{\rm H,0} = 0.1$, 1, and 10 cm^{-3}, assuming that the gas in the CSM has the solar composition and is fully ionized. For the other CSM density profile, we consider the density structure produced by the steady stellar wind during the evolution of the progenitor; the density profile is represented in terms of hydrogen number density as

$$n_{\rm H}(r) = n_{\rm H,1}\left(\frac{r}{r_1}\right)^{-2}\ {\rm cm}^{-3} \quad {\rm for} \quad r < r_2$$
$$= 1\,{\rm cm}^{-3} \quad {\rm for} \quad r \geqslant r_2, \tag{1}$$

where $r_1 = 1.2 \times 10^{18}$ cm is the radius of the freely expanding outermost ejecta at $t = 10$ yr after the explosion in the present model, and r_2 is the radius such that $n_{\rm H,1}(r_2/r_1)^{-2} = 1$ cm^{-3}. The coefficient $n_{\rm H,1}$ is given as

$$n_{\rm H,1} = n_{\rm H}(r_1) = \frac{\dot{M} A_{\rm H}}{4\pi r_1^2 v_w \mu m_{\rm H}}, \tag{2}$$

where $\dot{M}$ is the mass-loss rate, v_w is the stellar wind velocity, μ is the mean molecular weight, and $m_{\rm H}$ and $A_{\rm H}$ are the mass and the number abundance of the hydrogen atom, respectively. In the calculations, we consider three cases of $n_{\rm H,1} = 30$, 120, and 200 cm^{-3}; for example, the case of $n_{\rm H,1} = 30$ cm^{-3} with $v_w = 10$ km s^{-1} corresponds to $\dot{M} = 2 \times 10^{-5} M_\odot$ yr^{-1}, which is the mass-loss rate of Cas A's progenitor suggested from the analysis of shock dynamics by Chevalier & Oishi (2003).

The CSM models used in the calculations are listed in Table 3, and the uniform CSM and the stellar wind CSM ($\rho \propto r^{-2}$) are referred to as models A and B, respectively, with the value of $n_{\rm H,0}$ or $n_{\rm H,1}$ attached for each case. In the calculations, the spatial bin for hydrodynamic calculation is linearly divided into 2510 bins, and the size bin of dust is logarithmically divided into 80 bins for the range of 1 Å to 1 μm. We assume that the gas in the CSM has a temperature of 10^4 K and that the ejecta collide with the CSM at $t = 10$ yr after the SN explosion. We have confirmed that moderate changes in the CSM gas temperature

Table 3
Results of the Dust Evolution Calculation for Each CSM Model

CSM model	$t_{\rm coll}^{\rm He}$ (yr)	$t_{\rm coll}^{\rm O}$ (yr)	$t_{\rm coll}^{\rm Si}$ (yr)	$M_{\rm surv}$ ($M_\odot$)	η ($M_{\rm surv}/M_{\rm d}$)	$R_{\rm rev}^{330}$ (pc)	$R_{\rm forw}^{330}$ (pc)	$M_{\rm warm}^{330}$ ($M_\odot$)	$M_{\rm cool}^{330}$ ($M_\odot$)
(1)	(2)	(3)	(4)	(5)	(6)	(7)	(8)	(9)	(10)
A0.1	335	1300	3400	1.3×10^{-4}	7.8×10^{-4}	2.76	3.46	0.0	0.167
A1	155	590	1550	0.0	0.0	1.98	2.52	1.0×10^{-4}	0.167
A10	75	270	700	0.0	0.0	1.32	1.83	0.038	0.094
B30	63	340	1850	0.0	0.0	1.51	2.20	0.048	0.111
B120	48	150	560	0.0	0.0	0.93	1.67	0.008	0.072
B200	45	120	370	0.0	0.0	0.70	1.50	0.028	0.011

Notes. Column 1: name of the CSM models considered in this paper. Labels A and B represent the uniform CSM and the stellar wind CSM ($\rho \propto r^{-2}$), respectively, and the attached number denotes the value of $n_{\rm H,0}$ for model A and $n_{\rm H,1}$ model B (see the text). Columns 2–4: times at which the reverse shock encounters the He core, O-rich layer, and Si-rich layer, respectively. Column 5: mass of surviving dust at $t = 10^6$ yr. Column 6: ratio of surviving dust mass $M_{\rm surv}$ to the initial dust mass M_d. Columns 7 and 8: radii of the reverse and forward shocks at $t = 330$ yr. Column 9: mass of warm dust heated up by the shock at $t = 330$ yr. Column 10: mass of unshocked cold dust at $t = 330$ yr.

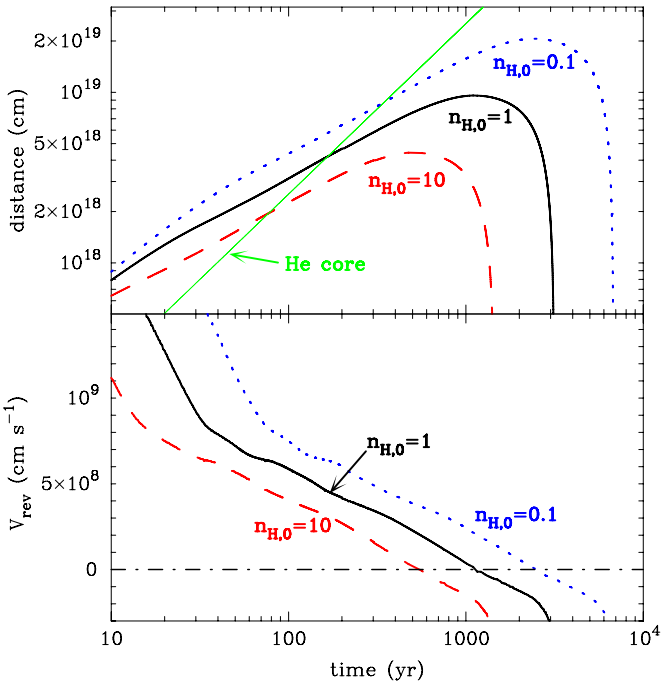

Figure 4. Time evolution of radius (upper panel) and velocity (lower panel) of the reverse shock for the uniform CSM models A0.1 (dotted), A1 (solid), and A10 (dashed) with $n_{\rm H,0} = 0.1$, 1, and 10 cm^{-3}, respectively. The trajectory of the boundary between the He core and the hydrogen envelope is depicted by the thin solid line in the upper panel, where the boundary is assumed not to be decelerated after the collision with the reverse shock for illustration.

(A color version of this figure is available in the online journal.)

($\sim 10^3$–10^5 K) do not influence the results of the calculations. The calculations are performed up to $t = 10^5$–10^6 yr, depending on the CSM density.

3.2. Results of Dust Evolution Calculation

3.2.1. Penetration of the Reverse Shock into the Ejecta

We first describe how the penetration of the reverse shock depends on the gas density in the CSM. Figure 4 exhibits the time evolution of the radius and the velocity of the reverse shock for the uniform CSM models A0.1, A1, and A10 with $n_{\rm H,0} =$ 0.1, 1, and 10 cm^{-3}, respectively. In the upper panel, we also show the trajectory of the boundary between the He core and the hydrogen envelope for a reference, assuming that the boundary is not decelerated even after the collision with the reverse shock.

The interaction of the SN ejecta with the ambient medium generates the forward shock running into the CSM to compress the ambient medium. The shocked hot ambient gas thrusts the ejecta in turn, driving the reverse shock that propagates into the ejecta but initially expands outward in the Eulerian coordinate. For the higher CSM density, the forward shock acquires a lower velocity, and the denser shocked gas is produced behind the forward shock. Accordingly, the reverse shock travels through the ejecta with a smaller outward velocity so that the unshocked ejecta can catch up with the reverse shock at earlier times (see Figure 4). Thus, the time at which the reverse shock collides with the He core is earlier for the higher gas density in the CSM: $t_{\rm coll} = 355$ yr, 155 yr, and 75 yr for the models A0.1, A1, and A10, respectively. For the stellar wind CSM, the collision times are earlier than for the uniform CSM models because of higher ambient density at the time of the ejecta–CSM interaction: $t_{\rm coll} =$ 63 yr, 48 yr, and 45 yr for the models B30, B120, and B200 respectively with $n_{\rm H,1} = 30$, 120, and 200 cm^{-3} (see Table 3).

Note that these collision times for the remnant of Type IIb SN (hereafter Type IIb SNR) are a few tens times earlier than those for Type II-P SNRs, for which $t_{\rm coll} = (1.5$–$10) \times 10^3$ yr for the CSM densities of $n_{\rm H,0} = 10$–0.1 cm^{-3} (Nozawa et al. 2007). The earlier arrival of the reverse shock at the He core in Type IIb SNRs is due to their much thinner hydrogen envelope and higher expansion velocity of the He core (see Figure 2(c)) than those of Type II-P SNRs. As shown below, the thickness of the hydrogen envelope has great effects on the evolution of dust in SNRs.

3.2.2. Destruction of Dust for the Uniform CSM

Figure 5 shows the time evolution of gas density (upper panel) and temperature (lower panel) within Type IIb SNR for the model A10 (uniform CSM with $n_{\rm H,0} = 10$ cm^{-3}). The gas densities behind the reverse and forward shocks, whose positions are depicted by the downward- and upward-pointing arrows in the lower panel, respectively, increase by a factor of about 4, compared with the unshocked ones. The temperature of the gas swept up by both the shocks rises to $>10^7$ K and remains over 10^6 K by $t \gtrsim 10^5$ yr. Dust grains staying in this hot gas are subject to destruction by sputtering.

Figure 6 presents the time evolution of positions (upper panel) and radii (lower panel) of dust grains with initial radii

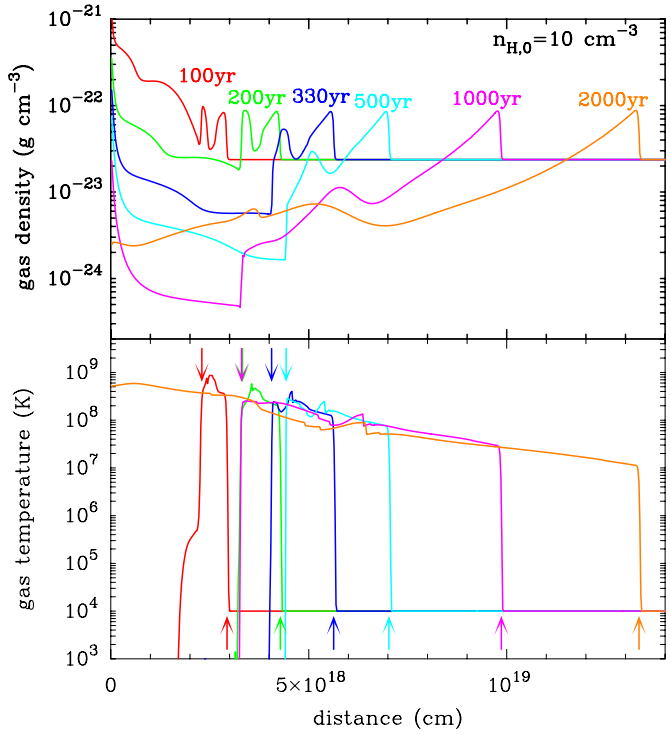

Figure 5. Structures of density (upper panel) and temperature (lower panel) of the gas at given times within the Type IIb SNR for the model A10 with $n_{H,0} = 10$ cm^{-3}. The positions of the forward and reverse shocks are indicated by the upward- and downward-pointing arrows in the lower panel, respectively.

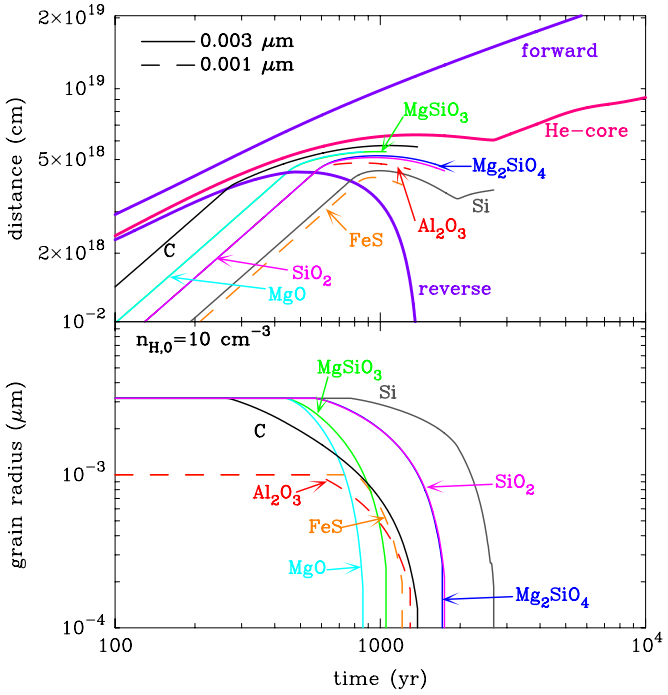

Figure 6. Time evolutions of the positions (upper panel) and radii (lower panel) of dust grains within the Type II SNR for the model A10. The initial radii of grains shown in the figures are 0.001 μm for Al_2O_3 and FeS (dashed lines) and 0.003 μm for C, $MgSiO_3$, Mg_2SiO_4, SiO_2, MgO, and Si (solid lines). The trajectories of the reverse and forward shocks as well as the position of the boundary between the He core and the hydrogen envelope are depicted by the thick curves in the upper panel.

of 0.001 μm (for Al_2O_3 and FeS) and 0.003 μm (for the other grains) for the model A10, together with the trajectories of the reverse and forward shocks in the upper panel. In this model, the reverse shock encounters the He layer at $t = 75$ yr, the O-rich layer at $t = 270$ yr, and the Si-rich layer at $t = 700$ yr. Once newly formed dust grains intrude into the shocked gas, they are efficiently decelerated by the gas drag and are quickly trapped in the hot plasma. These grains are completely destroyed and are not injected into the ISM. Actually, all newly formed grains are destroyed in the postshock gas for most of the models considered in this paper. One of the reasons for this is that the radii of newly formed grains are very small; since the deceleration rate of dust is inversely proportional to the grain radius (e.g., Nozawa et al. 2007), dust grains with radii of <0.01 μm are easily captured by the shock-heated gas and are destroyed by thermal sputtering. Another reason is that the reverse shock can reach the He core more than 20 times earlier for SNe IIb than for SNe II-P as mentioned above; although the initial gas density in the ejecta of the SN IIb is three orders of magnitude lower than those in SNe II-P (see Figure 2(b)), at such an early time, the gas density in the He core of the SN IIb is still higher by a factor of ∼10 than those in SNe II-P at several thousand years. This leads to frequent collisions between dust and gas and causes the efficient deceleration and destruction of dust.

In Figure 7(a), we compare the time evolution of the total dust mass for the uniform CSM with $n_{H,0} = 0.1$, 1, and 10 cm^{-3}. We can see that dust grains are destroyed more efficiently and quickly at higher CSM density. This is because the increase of the gas density in the CSM leads to the earlier arrival of the reverse shock at the dust-forming region, which keeps the gas density in the He core high enough for dust grains to be eroded by sputtering efficiently. For $n_{H,0} = 0.1$ cm^{-3}, C grains of $\sim 10^{-4}\ M_\odot$ can survive for $t = 10^6$ yr, while all dust grains are destroyed within $t = 4 \times 10^5$ yr for $n_{H,0} = 1$ cm^{-3} and $t = 5 \times 10^3$ yr for $n_{H,0} = 10$ cm^{-3}.

3.2.3. Destruction of Dust for the Stellar Wind CSM

Figure 7(b) shows the evolution of the total dust mass in SNRs for the stellar wind CSM ($\rho \propto r^{-2}$) models. For these models, dust grains are completely destroyed before $t = 10^5$ yr. However, the evolution of dust in SNRs shows the different behaviors as shown in Figures 8(a) and (b), where the time evolutions of mass of each dust species for the models B30 and B120 are presented. For model B30 with $n_{H,1} = 30$ cm^{-3}, a small amount of C grains survive after $t = 10^4$ yr, whereas the other grain species are completely destroyed before $t \sim 10^4$ yr. In the case of model B120 with the CSM gas density four times higher than that for B30, C grains are destroyed quickly after the collision with the reverse shock, whereas the masses of some dust species such as SiO_2 and Si grains decrease more slowly than those for B30.

In order to explain these different behaviors of dust evolution, we show the time evolutions of density structure within SNRs for B30 and B120 in Figures 9(a) and (b), respectively. Since the deceleration and erosion rates are dependent on the ion number density, the time evolutions of the total ion number density, n, are given in the lower panel in Figure 9, along with the positions of C, SiO_2, and Si grains with the initial radii of 0.003 μm. We also present the time evolutions of positions and radii of these C, SiO_2, and Si grains in Figure 10.

For model B30 (Figures 9(a) and 10(a)), the SNR expands into the CSM with the density profile of $\rho \propto r^{-2}$ during only 340 yr, and then propagates into the ISM with a constant density of $n_H = 1$ cm^{-3}. Thus, one might guess that the evolution of dust in the SNR would be quite similar to that for model A1 with

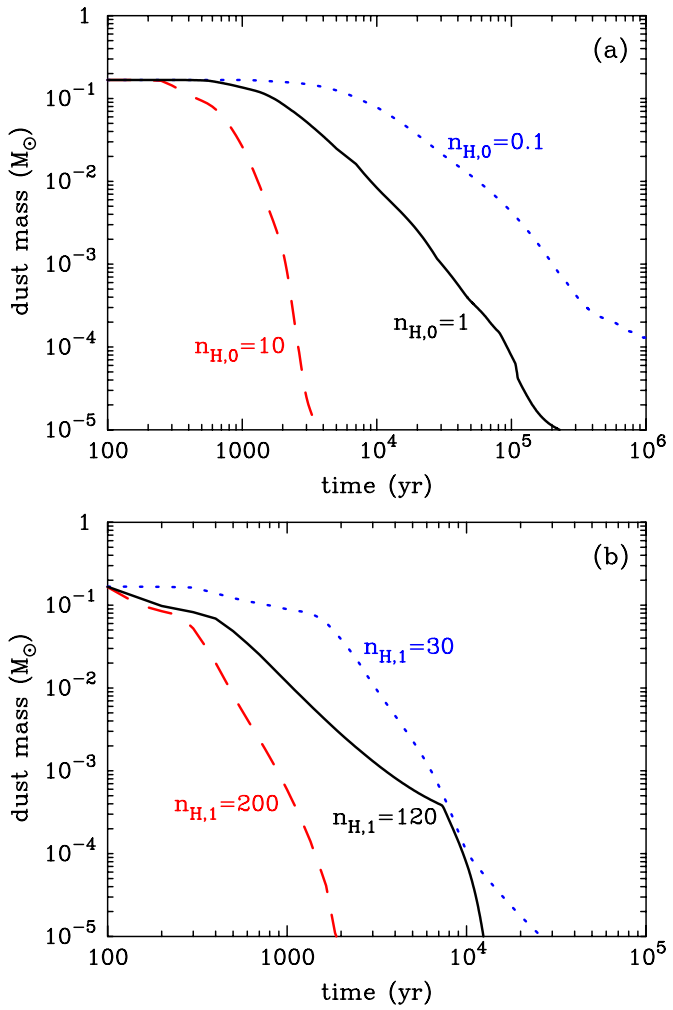

Figure 7. Time evolutions of the total dust mass inside the Type IIb SNRs running into (a) the uniform CSM with $n_{\rm H,0} = 0.1$ cm^{-3} (dotted), 1 cm^{-3} (solid), and 10 cm^{-3} (dashed), and (b) the stellar wind CSM with $n_{\rm H,1} = 30$ cm^{-3} (dotted), 120 cm^{-3} (solid), and 200 cm^{-3} (dashed).

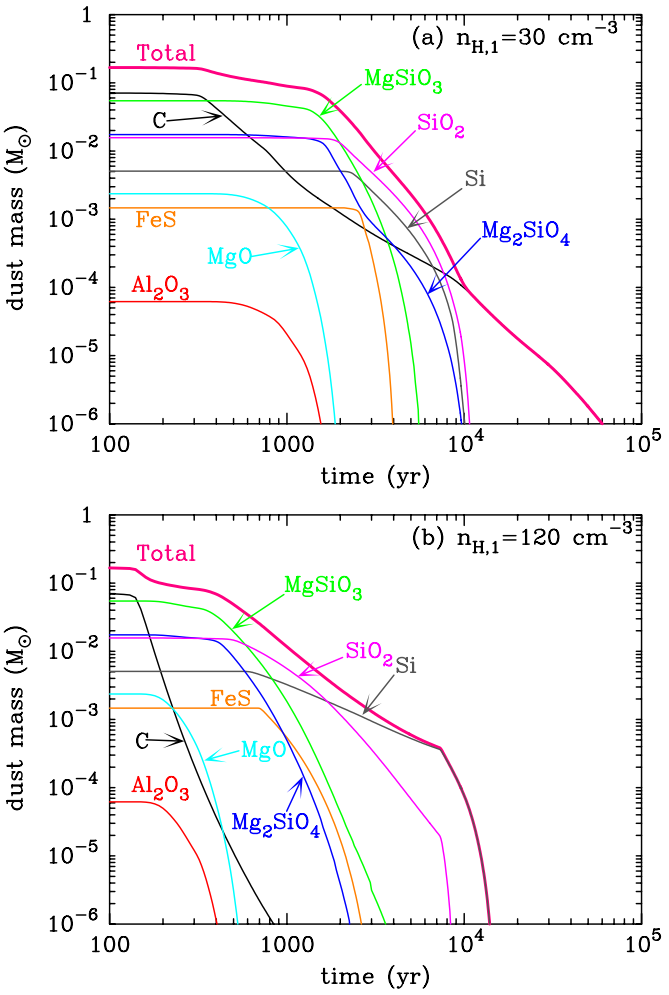

Figure 8. Time evolution of the mass of each dust species inside the Type IIb SNRs running into the stellar wind CSM with the density profile of $\rho \propto r^{-2}$ for (a) $n_{\rm H,1} = 30$ cm^{-3} and (b) $n_{\rm H,1} = 120$ cm^{-3}. The thick solid line indicates the time evolution of the total dust mass.

the uniform CSM of $n_{\rm H,0} = 1$ cm^{-3}. However, as presented in Figure 7, dust grains in the ejecta are completely destroyed about 10 times earlier for B30 than for A1, because the gas density behind the reverse shock for B30 is about 8 times higher than for A1 at $t \lesssim 340$ yr due to the fast passage of the reverse shock into the ejecta (see Table 3). In addition, the density of gas in the region swept up by the reverse shock at the initial phase remains quite high ($n \gtrsim 0.3$ cm^{-3}) even after $t = 3000$ yr (see Figure 9(a); hereafter, such a region is referred to as the dense gas region). As can be seen in Figure 10(a), dust grains are trapped in the dense gas region shortly after their collisions with the reverse shock and are completely destroyed by thermal sputtering. C grains formed in the inner C-rich region of the He layer collide with the reverse shock at an early epoch ($t \simeq 330$ yr) and are eroded by sputtering in the denser gas than those for SiO_2 and Si grains formed inside the O-rich layer. However, C grains can survive for a relatively long period, compared with SiO_2 and Si grains (see Figure 8(a)), because the erosion rate of C grains is smaller than the other grain species by a factor of about 5 (Nozawa et al. 2006).

In the case of model B120 (Figures 9(b) and 10(b)), the reverse shock more quickly penetrates into the ejecta than B30, which results in an extended shocked region between the reverse shock front and the dense gas region (see Figure 9(b)). C grains collide with the reverse shock at $t \simeq 140$ yr and are immediately destroyed in the shocked gas with $(330/140)^3 \simeq 13$ times higher density than that for B30. SiO_2 and Si grains, which encounter the reverse shock at $t \simeq 400$ yr and $t \simeq 700$ yr, respectively, intrude into the 30–40 times denser postshock gas than the cases for B30. However, the gas density is not high enough for the SiO_2 and Si grains to be trapped and completely destroyed. Instead, upon collisions with the reverse shock, these grains are greatly decelerated by the gas behind the reverse shock, which prevents them from reaching the dense gas region in a short time; SiO_2 grains are finally trapped in the extended shocked region and are destroyed without arriving at the dense gas region. Si grains are eroded slowly passing through the extended shocked region until they reach the dense gas region at 10^4 yr.

For model B200, the reverse shock can propagate into the ejecta even earlier than B120. Hence, the gas density behind the reverse shock is so high that all grain species are trapped and are quickly destroyed once they are swept up by the reverse shock. These results demonstrate that the evolution of dust within SNRs strongly depends on the gas density and structure in the CSM, as well as on the composition of dust grains and their initial position in the ejecta.

In Table 3, we summarize the total mass $M_{\rm surv}$ of surviving dust in Type IIb SNRs at $t = 10^6$ yr for the CSM models

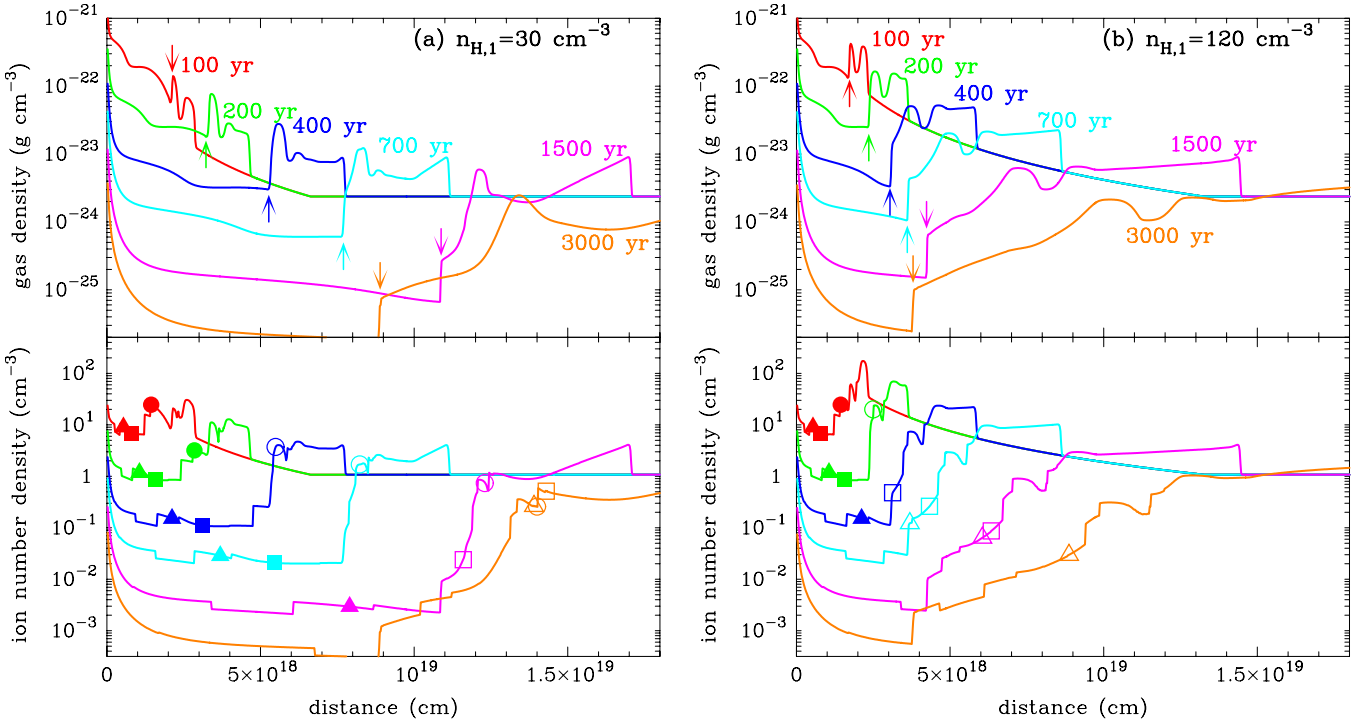

Figure 9. Time evolutions of the gas density (upper panel) and the corresponding total ion number density (lower panel) as a function of distance from the center for (a) $n_{H,1} = 30$ cm^{-3} and (b) $n_{H,1} = 120$ cm^{-3}. The positions of the reverse shock are indicated by the arrows in the upper panels. In the lower panels, the positions of C (circles), SiO_2 (squares), and Si grains (triangles) are plotted where the filled and opened symbols denote the unshocked and shocked ones, respectively.

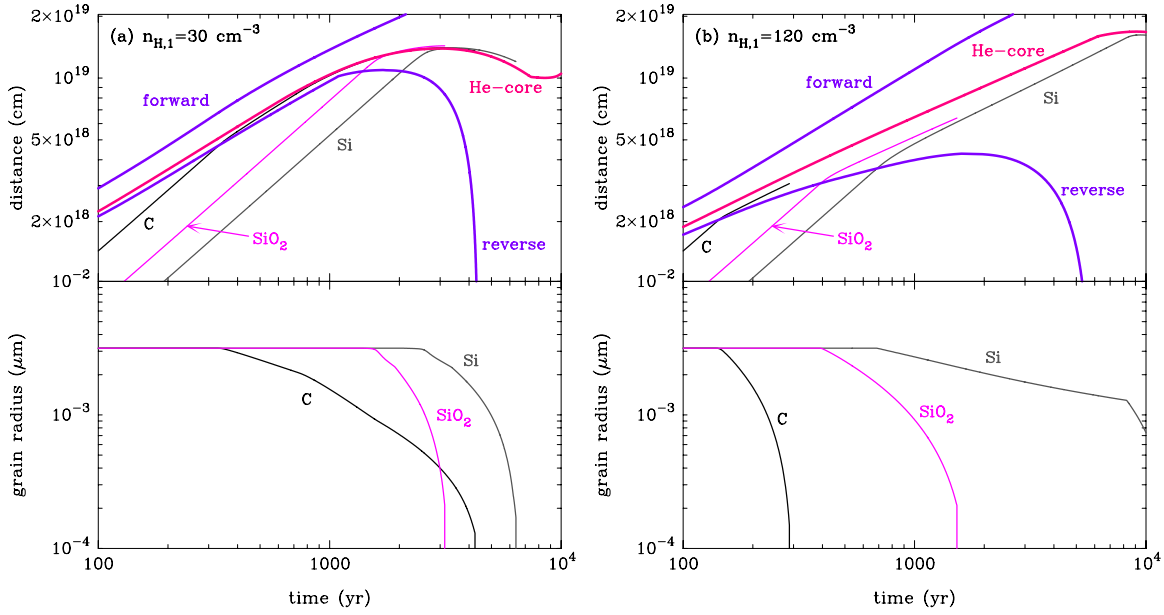

Figure 10. Time evolutions of the positions (upper panel) and radii (lower panel) of C, SiO_2, and Si grains with the initial radii of 0.003 μm in the Type IIb SNR for (a) $n_{H,1} = 30$ cm^{-3} and (b) $n_{H,1} = 120$ cm^{-3}. The trajectories of the reverse and forward shocks as well as the position of the surface of the He core are depicted by the thick curves in the upper panel.

considered in this paper. For all CSM models except for model A0.1, dust grains formed in the ejecta are completely destroyed before $t = 10^6$ yr. Even for model A0.1, the destruction efficiency η, defined as the ratio of M_{surv} to the initial dust mass M_d, is less than 10^{-3}, in contrast to the case of SNe II-P with thick hydrogen envelopes, for which 2%–80% of dust grains can survive for the ISM with $n_{H,0} = 10$–0.1 cm^{-3} (Nozawa et al. 2007). As shown above, the difference in the evolution of dust between Type IIb and Type II-P SNRs is caused by the thickness of the outer envelope; for SNe II-P retaining a massive hydrogen envelope, the radii of newly formed grains are larger than 0.01 μm, and the arrival time of the reverse shock at the dust-forming region inside the He core is retarded, both of which act against the destruction of dust grains by sputtering. Therefore, the amount of dust injected into the ISM strongly depends on the type of SNe through the varying thicknesses of their outer envelopes, even if a large amount of dust grains can form in the ejecta of CCSNe. From the results of the present calculations, we conclude that low-mass envelope SNe such as SNe IIb and SNe Ib/c cannot be major contributors of interstellar

dust as long as the gas density in the CSM is not too low ($n_{\rm H} \ll 0.1$ cm^{-3}).

4. IR THERMAL EMISSION FROM DUST IN TYPE IIb SNRs

Dust grains bathed in the shocked gas inside SNRs are heated up by collisions with the hot gas and emit their thermal radiation at IR wavelengths. If the collisional heating rate and radiative cooling rate of dust are balanced, the dust can reach equilibrium temperature. However, in a rarefied hot plasma such as SNRs, small-sized dust grains undergo stochastic heating, which influences the emissivity and the resulting SED (e.g., Dwek 1986). In this section, based on the results of the simulations of dust evolution presented in Section 3 and taking into account stochastic heating, we calculate the SED by thermal emission from shock-heated dust within SNRs. The SNRs are placed at a distance of 3.4 kpc in order to compare with the observations of Cas A SNR in the next section.

4.1. Calculation of Stochastic Heating

The heating and thermal emission of dust are calculated by using the output of the dust evolution simulations: density and temperature of the gas as well as size, velocity relative to the gas, and number density of each dust species in each spatial bin as a function of time. We employ a Monte Carlo method to calculate the temperature distribution functions of dust grains by stochastic heating. In the calculations, we consider only collisions with electrons for the heating of dust; under the present situation in which dust grains are quickly trapped in the hot gas, collisions with ions are much less frequent, and the heating of dust is dominated by collisions with electrons.

The fraction of incident energy that is deposited into a grain is calculated following the prescription by Dwek (1987), and the stopping range of an electron for each grain species is calculated by the approximation formula derived on the basis of those by Tabata et al. (1972) and Iskef et al. (1983). The heat capacity of each grain species is taken from Takeuchi et al. (2005), and the optical constants are taken from the following sources: C (Edoh 1983), Al_2O_3 (Toon et al. 1976 for $\lambda \leqslant 8\,\mu$m and Begemann et al. 1997 for $\lambda > 8\,\mu$m), $MgSiO_3$ (Dorschner et al. 1995; but the optical constants of Mg_2SiO_4 are used for $\lambda \leqslant 0.3\,\mu$m, see Hirashita et al. 2008), Mg_2SiO_4 (Semenov et al. 2003), SiO_2 (Philipp 1985), MgO (Roessler & Huffman 1991), FeS (Semenov et al. 2003), and Si (Piller 1985). We re-bin the sizes of dust into 12 bins from 1 Å to 0.1 μm and divide the shocked region into 20 spatial bins weighted by the mass of the gas, because the calculation is too time-consuming. We have verified that even if the number of re-binned size (spatial) bins increases to 20 (50), the resulting SEDs are virtually the same.

4.2. Time Evolution of Thermal Emission from Dust

Figures 11–14 show the time evolution of SEDs by thermal emission from shocked dust for different CSM models every 200 yr in the range from 200 yr to 1800 yr after the explosion. In these figures, the solid curves display the SEDs taking into account stochastic heating, and the dashed curves the SEDs calculated by assuming the equilibrium without stochastic heating. We can see that the SEDs taking account of stochastic heating are strongly different from those with the equilibrium temperatures, especially at wavelengths shorter than $\lambda = 20\,\mu$m. This implies that the effect of stochastic heating is very important in modeling the IR SED by dust emission within SNRs, as demonstrated by Dwek (1986).

For model A1 with uniform gas density (Figure 11), the reverse shock hits the He core at $t = 155$ yr after the explosion. The mass of C grains formed in the outer C-rich region of the He layer is too small ($<5 \times 10^{-4}\,M_\odot$) to emit the thermal emission significantly during $t = 200$–400 yr. At $t > 400$ yr, thermal emission from a large amount of C grains formed in the inner C-rich part of the He layer always dominates the SED, because the gas density in the SNR is not high enough to destroy C grains efficiently. The reverse shock reaches the O-rich layer at $t \simeq 600$ yr, but the emission features of silicate and oxide grains are inconspicuous, being overwhelmed by thermal emission from C grains.

For the higher CSM density of model A10 (Figure 12), C grains are more efficiently destroyed by sputtering than those in model A1, and the emission features from other dust species grow prominent with time. The reverse shock encounters the O-rich layer at $t = 270$ yr, and the emission feature of Mg-silicates ($MgSiO_3$ and Mg_2SiO_4) around $\lambda = 10\,\mu$m begins to be noticeable at $t = 600$ yr. The feature of SiO_2 at $\lambda = 20\,\mu$m is outstanding after $t = 800$ yr, and the emission features from Si and FeS grains appear after $t = 1200$ yr. Because of the efficient destruction of dust, the thermal emission continues to decrease with time.

In the case of model B30 with the stellar wind's density profile (Figure 13), the reverse shock collides with the He core at $t = 63$ yr, which is earlier than in model A10. Thermal emission from C grains dominates the SED by $t \sim 1000$ yr, and after that the contributions from Mg-silicates become recognizable. However, stochastic heating of small C grains still contributes to the SED at $\lambda \lesssim 10\,\mu$m, because some C grains can survive even after $t = 1000$ yr owing to the low gas density ($n_{\rm H} = 1$ cm^{-3}) at a large distance in comparison with model A10. We can see that the flux densities significantly increase between 1200 yr and 1400 yr in this model. This is due to the fact that during this time interval, the reverse shock has swept up the ejecta region where a large amount of silicate grains are formed ($M_r \simeq 1.8\,M_\odot$, see Figure 3(a)). The dust grains swept up by the shocks continue to be eroded by sputtering, while the reverse shock continues to intrude into the inner He core and to supply newly formed dust grains to the shocked gas. Thus, the time evolution of SEDs is determined by the balance between the amount of dust destroyed in the hot gas and the amount of dust swept up by the reverse shock.

For model B120 (Figure 14), the reverse shock can quickly propagate into the ejecta, and arrives at the He core, O-rich layer, and Si-rich layers at $t = 48$ yr, 150 yr, and 560 yr, respectively. Thus, we can see the quick evolution of the SED characterized by the features of various grain species. Since the gas density is significantly high, especially at an early phase, C grains are quickly destroyed as can be seen from the evolution of SED at $\lambda \lesssim 8\,\mu$m, and the emission from stochastically heated small C grains disappears at $t \gtrsim 600$ yr.

The results of these calculations clearly demonstrate that the time evolutions of IR emission from dust heated up in SNRs are sensitive to the density of gas as well as the density profile in the surrounding medium. The ambient gas density controls the passage of the reverse shock into the ejecta and affects the destruction by sputtering and stochastic heating of dust in the hot gas. Hence, the resulting IR SED reflects the evolution of dust in SNRs and also holds key information on the density structure in the ambient medium. In other words, the temporal evolution

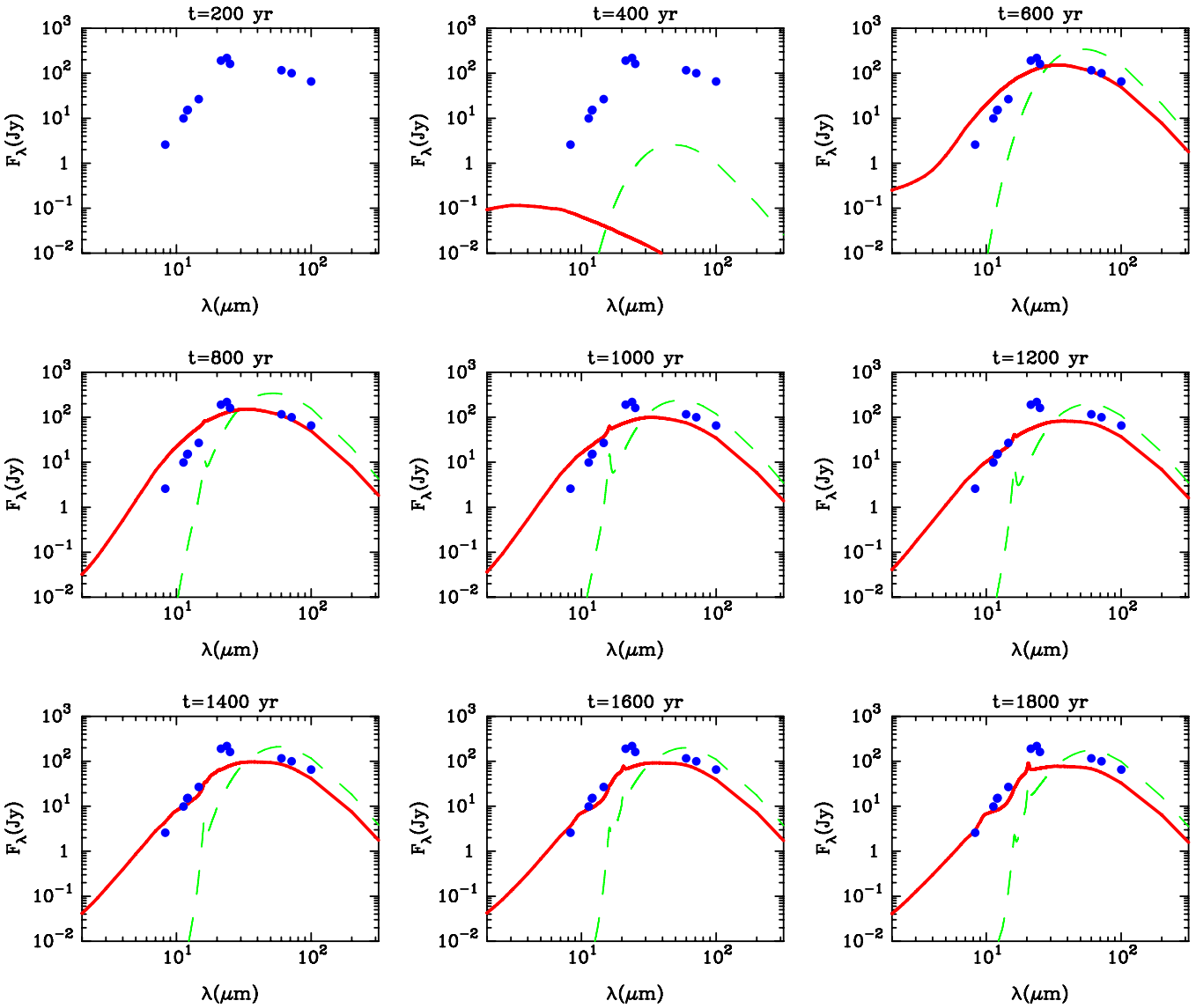

Figure 11. Time evolution of SEDs by thermal emission from shocked-heated dust within the Type IIb SNR for the uniform CSM model A1 ($n_{\rm H,0} = 1$ cm^{-3}) every 200 yr after the explosion. The solid and dashed lines show the IR thermal emission with and without stochastic heating, respectively. The data points are the syncrotron-subtracted flux densities observed for Cas A and are taken from Hines et al. (2004).

(A color version of this figure is available in the online journal.)

of SED from dust in shock-heated gas can be a very useful tool for investigating the properties of dust in SNRs as well as the density structure in the CSM and thus the mass-loss history of the progenitor star during the late phase of its evolution.

5. APPLICATIONS TO THE Cas A SNR

In this section, we apply the results of our calculations for dust evolution and the resulting SEDs presented in Sections 3 and 4 to Cas A SNR, to gain insight into the composition and mass of dust residing in Cas A SNR as well as the mass-loss rate of the progenitor. After briefly summarizing the observed characteristics of Cas A relevant to this study, we present the comparison of the calculated SEDs with the observed one.

5.1. Cas A SNR

Cas A is one of the best studied Galactic SNRs at a broad range of wavelengths spanning from radio to γ-ray. Its estimated age is $\sim$330 yr (Fesen et al. 2006a; Thorstensen et al. 2001), and the distance to Cas A is determined to be 3.4 kpc from the proper motion of fast moving knots (FMKs; Reed et al. 1995). The X-ray observations with *Chandra* have resolved the radii of the reverse and forward shocks to be $95'' \pm 10''$ and $153'' \pm 12''$, respectively (Gotthelf et al. 2001), which correspond to $R_{\rm rev}^{330} = 1.57 \pm 0.17$ pc and $R_{\rm forw}^{330} = 2.52 \pm 0.19$ pc at a distance of 3.4 kpc.

Recently Krause et al. (2008) obtained an optical spectrum of the Cas A SN around the maximum brightness via the scattered light echo, and concluded that the Cas A SN was of Type IIb, originating from a supergiant that had lost most of its hydrogen envelope prior to the explosion as has been suggested by the close binary scenario for SNe IIb (e.g., Nomoto et al. 1995). The numerical simulations (Chevalier & Oishi 2003; Young et al. 2006) and the discovery of FMKs containing some hydrogen (Fesen & Becker 1991; Fesen 2001) also seem to strongly support this conclusion.

The presence of dust formed in the ejecta has been confirmed by IR observations with the *IRAS* (Dwek et al. 1987), the *ISO*

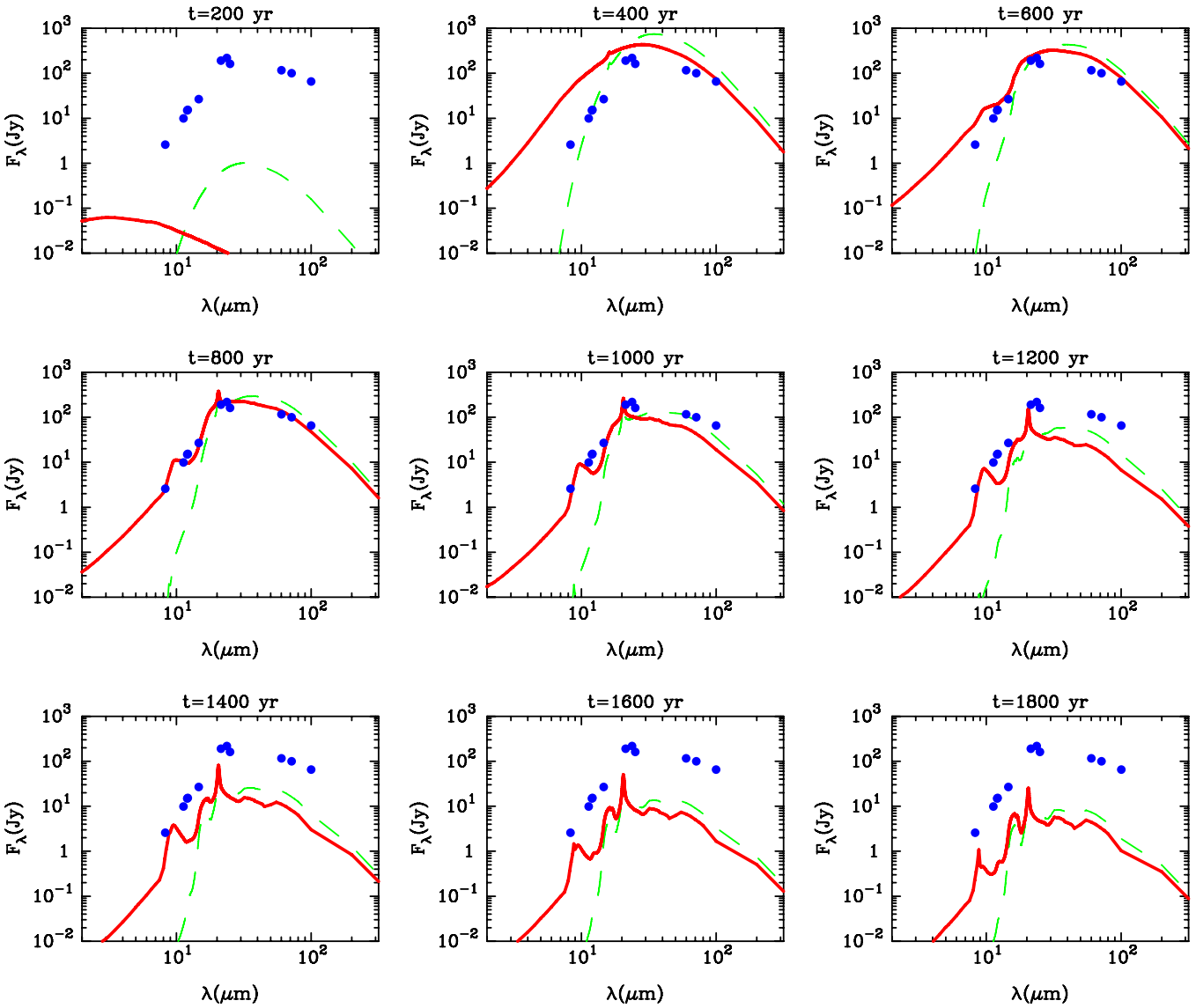

Figure 12. Same as Figure 11, but for model A10 ($n_{\rm H,0} = 10$ cm^{-3}).
(A color version of this figure is available in the online journal.)

(Lagage et al. 1996), and *Spitzer* (Hines et al. 2004). The IR spectra of FMKs taken by the *ISO* allowed us to examine the composition of dust, leading to the conclusion that the main species of newly formed dust in Cas A are silicate and/or oxide grains (Arendt et al. 1999; Douvion et al. 2001).

There has been a continuing controversy about the amount of dust residing in Cas A SNR; the dust mass derived from the observations described above was smaller than $3 \times 10^{-3}\,M_\odot$. Rho et al. (2008) estimated the mass of dust to be 0.02–0.054 $M_\odot$ from the spectral mapping covering the entire region of Cas A by the *Spitzer*. Based on submillimeter (submm) observation with the SCUBA, Dunne et al. (2003) have reported the detection of 2–4 $M_\odot$ of cold dust in Cas A. Dwek (2004) ascribed this cold dust emission to metallic needles of $<10^{-3}\,M_\odot$ formed in the ejecta. On the other hand, the MIPS 160 μm map of Cas A, complemented by CO and OH line observations, have demonstrated that the detected submm emission originated from interstellar dust in the foreground molecular clouds (Krause et al. 2004), and the mass of cold dust associated with Cas A is estimated at most to be 0.2 $M_\odot$ (Krause et al. 2004) and 1.5 $M_\odot$ (Wilson & Batrla 2005).

Although the existence of a peculiar species of cold dust with $\sim$1 $M_\odot$ is also proposed from submm polarization (Dunne et al. 2009), we do not consider here the measurements at wavelengths longer than 160 μm. In what follows, we compare the calculated SEDs with the synchrotron-subtracted IR flux densities at $\lambda =$ 8–100 μm taken from the photometric observations tabulated in Hines et al. (2004).

5.2. Comparison with the Observations of Cas A

5.2.1. IR Emission from Shock-heated Newly Formed Dust

We first compare the results for the uniform CSM with the observations of Cas A. For $n_{\rm H,0} = 1$ cm^{-3}, IR emission is dominated by stochastically heated small C grains throughout the age of the remnant, as shown in Section 4.2. This causes the excess emission over the observed SED at $\lambda \lesssim 15\,\mu$m until $t = 1000$ yr, and the calculated SED cannot reproduce the observational data. The fact that the C grain-dominated IR SED does not match with the IR measurements of Cas A is also pointed out by Bianchi & Schneider (2007).

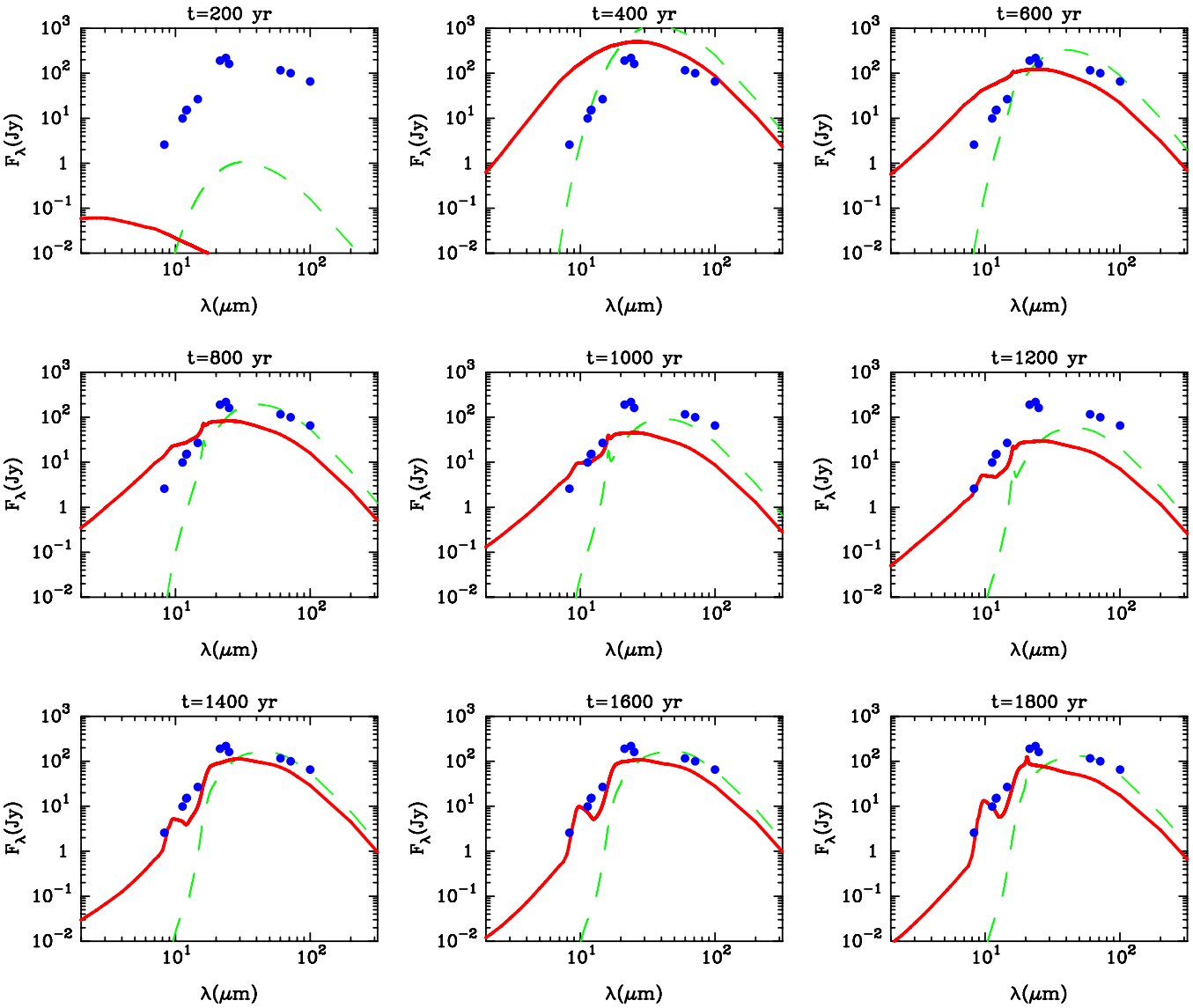

Figure 13. Same as Figure 11, but for the stellar wind CSM model B30 ($n_{\rm H,1} = 30$ cm^{-3}).
(A color version of this figure is available in the online journal.)

For the case of $n_{\rm H,0} = 10$ cm^{-3}, the calculated SED at $t = 800$ yr is in good agreement with the IR observations of Cas A (see Figure 12). The mass of shock-heated dust at $t = 800$ yr is 0.048 $M_\odot$, which is consistent with the dust mass of 0.02–0.054 $M_\odot$ in Cas A estimated from the *Spitzer* observations (Rho et al. 2008). The comparison strongly suggests that the dominant species of dust responsible for the observed SED are silicate grains and that the reverse shock has already reached the inner O-rich layer in the ejecta. However, the remnant age of 800 yr is much older than the age of Cas A, and the SED at $t = 330$ yr does not agree with the observations. We also found that any uniform CSM models with gas density higher than $n_{\rm H,0} = 10$ cm^{-3} cannot reproduce the observed SED, partly because the dust grains are quickly destroyed and partly because the temperature of the dust is too high. Thus, we conclude that thermal emission of dust grains heated up in SNRs expanding into the uniform CSM cannot explain the observed IR SED of Cas A.

Next, we move to the comparison of the results for the CSM density structure of $\rho \propto r^{-2}$. Figures 15(a)–(c) present the calculated SEDs at $t = 330$ yr for $n_{\rm H,1} = 30$, 120, and 200 cm^{-3}. In these figures, we also show the contribution of each dust species to the total flux densities. Note that the SEDs calculated without stochastic heating are not shown in these figures, since they can never reproduce the observations of Cas A for any CSM models.

The case of $n_{\rm H,1} = 30$ cm^{-3} corresponds to $\dot{M} = 2 \times 10^{-5}\,M_\odot$ yr^{-1} for $v_w = 10$ km s^{-1}, and Chevalier & Oishi (2003) have suggested that the density structure reproduces the observed radii of the reverse and forward shocks derived from the X-ray observations (Gotthelf et al. 2001). Our simulation also approximately reproduces the observed shock radii for Cas A: 1.5 pc for the reverse shock and 2.2 pc for the forward shock. However, in this case, the reverse shock has not yet reached the O-rich layer at $t = 330$ yr (see Table 3). The calculated flux densities from the shock-heated C grains of $\sim$0.05 $M_\odot$ are much higher than the observations at the whole mid-IR wavelengths.

With $n_{\rm H,1} = 120$ cm^{-3}, the calculated SED reasonably reproduces the observed SED at $\lambda \lesssim 30\,\mu$m, although there is some discrepancy at $\lambda \simeq 12\,\mu$m. The SED also predicts

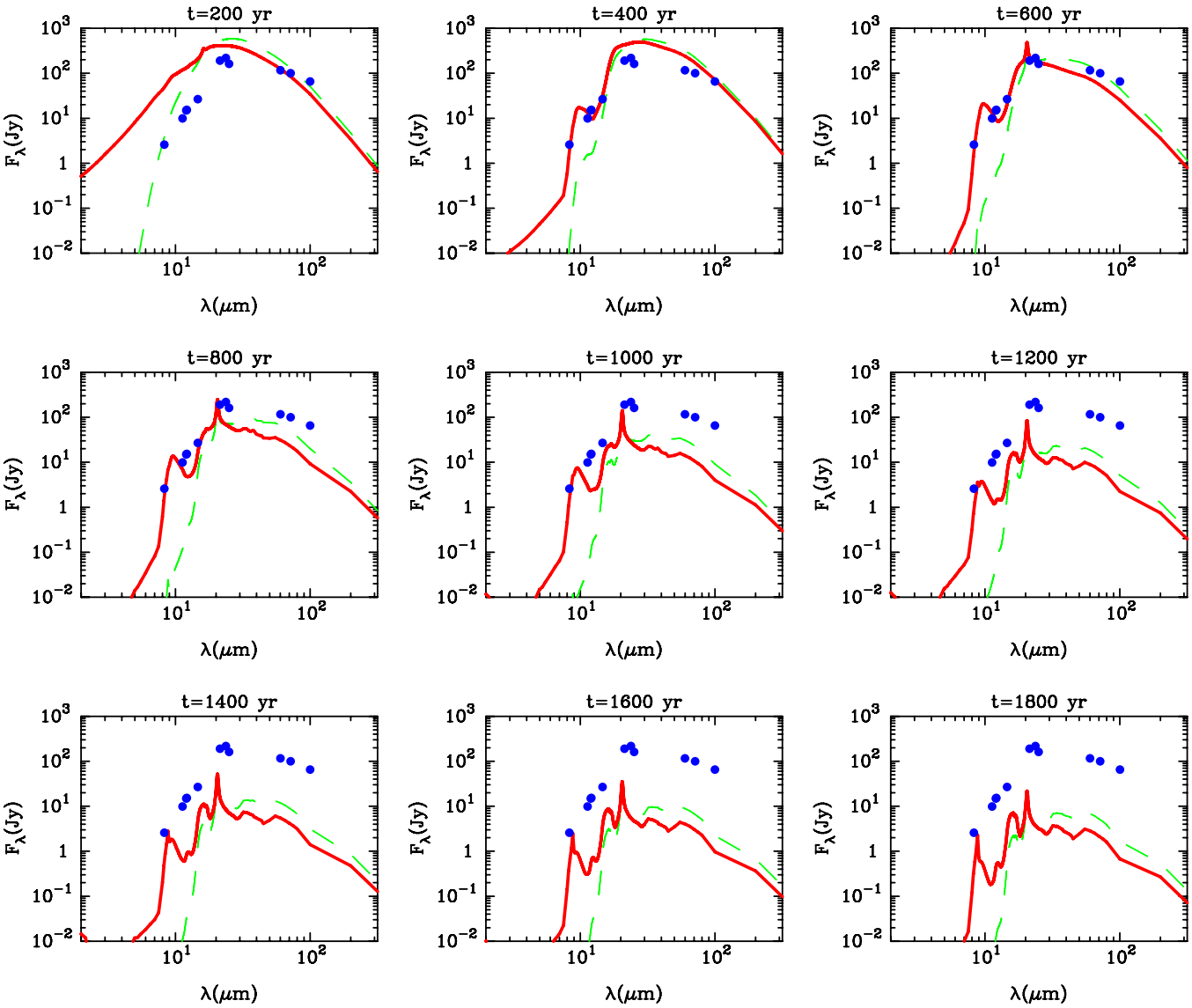

Figure 14. Same as Figure 11, but for model B120 ($n_{\rm H,1} = 120$ cm^{-3}).
(A color version of this figure is available in the online journal.)

the considerably lower flux densities at $\lambda \gtrsim 50\,\mu$m, which can be recovered by considering the unshocked dust as will be discussed later. The dust species most contributing to the SED is $MgSiO_3$, which is one of the major grain species in Cas A presumed from the IR spectra (Douvion et al. 2001; Rho et al. 2008). Mg_2SiO_4, SiO_2, and MgO grains more or less contribute to the SED, and C grains partly contribute at $\lambda \lesssim 15\,\mu$m as well. The total mass of shocked dust grains is 0.008 $M_\odot$, which is smaller than the estimate by Rho et al. (2008) but is larger than those from the other IR observations.

For $n_{\rm H,1} = 200$ cm^{-3}, the calculated SED does not match with the observations, especially at $\lambda = 20$–$60\,\mu$m. In this case, the reverse shock invades deeper layers in the ejecta and sweeps up a larger mass (0.028 $M_\odot$) of silicate grains, compared with the case of $n_{\rm H,1} = 120$ cm^{-3}. Therefore, the derived SED produces much higher flux densities than the observations. We also calculate the thermal emission from shocked dust for the CSM denser than $n_{\rm H,1} = 200$ cm^{-3}, but the outcomes suffer from much lower flux densities at $\lambda \gtrsim 30\,\mu$m because of the efficient destruction of dust and the relatively high temperature of dust. In addition, in such dense cases, the shock radii are much smaller than the observations. Hence, we conceive that the cases of $n_{\rm H,1} \gtrsim 200$ cm^{-3} are unlikely as the density structure around Cas A.

In summary, our results indicate that the stellar wind's density profile with $n_{\rm H,1} \simeq 120$ cm^{-3} is most favorable to account for the observed IR emission at the age of Cas A. The corresponding mass-loss rate $8 \times 10^{-5}\,M_\odot$ yr^{-1} is at most a factor of 4 higher than the mass-loss rates estimated for SNe IIb: (3–4) $\times 10^{-5}\,M_\odot$ yr^{-1} (Suzuki & Nomoto 1995; Fransson et al. 1996) deduced for SN 1993J (at $r \simeq 1 \times 10^{15}$ cm) and $2 \times 10^{-5}\,M_\odot$ yr^{-1} for Cas A (Chevalier & Oishi 2003). In view of the uncertainties involved in the density gradient and clumpiness in the CSM, these estimated mass-loss rates can be regarded as being consistent. On the other hand, the result for $n_{\rm H,1} = 120$ cm^{-3} predicts quite smaller shock radii than those for Cas A (see Table 3). The discrepancy in the shock radii as well as the mass-loss rate could be considered to be partly caused by the difference in the explosion energy and the thickness of the hydrogen envelope of the SN model used in this study.

It should be emphasized that the IR emission from newly formed dust grains that are heated up in the hot plasma inside

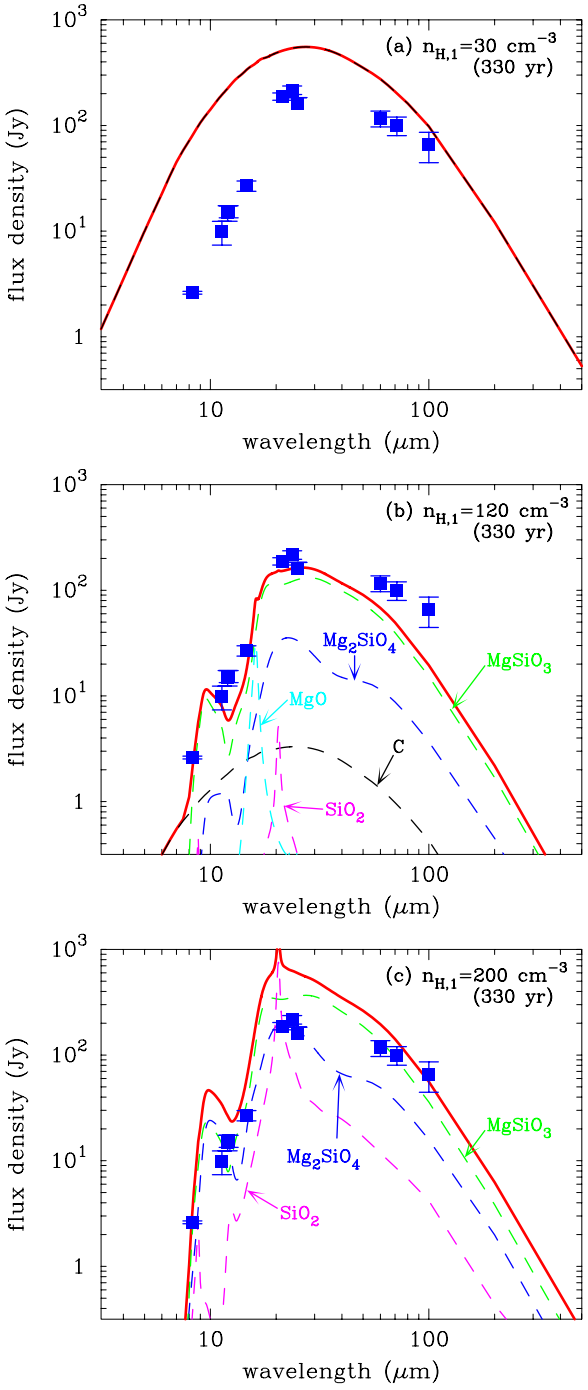

Figure 15. Comparison between the IR observations of Cas A and the calculated SEDs by thermal emission from shocked dust at 330 yr for (a) $n_{\rm H,1} = 30$ cm^{-3}, (b) 120 cm^{-3}, and (*c*) 200 cm^{-3}. The dashed lines indicate the contribution of each dust species. The IR flux densities in (a) are produced only by C grains. The data points are the same as in Figure 11.

(A color version of this figure is available in the online journal.)

SNRs can reproduce the mid-IR ($\lambda = 8$–$30\,\mu$m) SED of Cas A without any fine-tuning. On the other hand, the obtained results for $n_{\rm H,1} = 120$ cm^{-3} significantly underestimate the flux densities at longer wavelengths ($\lambda \gtrsim 50\,\mu$m). Although the thermal emission from cooler dust in the dense optically emitting knots is expected to mitigate this difference, modeling of such a dust emission may need a sophisticated radiative transfer simulation and is beyond the scope of this paper. Hereafter, we discuss the contributions from the following two potential sources to the observed SED at $\lambda \gtrsim 50\,\mu$m: (1) the circumstellar (CS) dust grains that were formed in the mass-loss wind during the evolution of the progenitor star and then were swept up by the forward shock and (2) the newly formed dust that were formed in the ejecta but have not been yet swept up by the reverse shock.

5.2.2. Contribution from Pre-existing CS Dust

In order to examine the contribution from the preexisting CS dust, we simulate the destruction and heating of the shocked CS dust for the density structure of the CSM corresponding to the mass-loss rate of $8 \times 10^{-5}\,M_\odot$ yr^{-1}. The composition of the CS dust is considered to be either carbonaceous or silicate depending on the C/O ratio in the stellar wind. Carbonaceous grains condense in C/O > 1, which is realized in the winds of carbon-rich Wolf–Rayet stars. Silicate grains are expected to form in the wind of a supergiant, where the abundance ratio of heavy elements is nearly solar with C/O < 1. Although a supergiant is a more likely progenitor of Cas A (Section 5.1), we consider here, as the dust composition in the CSM, both amorphous carbon and astronomical silicate, for which the optical constants are taken from Edo (1983) and Draine & Lee (1984), respectively. For the size distribution of the dust, we adopt the MRN size distribution ($n(a)da \propto a^{-3.5}da$; Mathis et al. 1977) with upper and lower limits of $a = 0.001\,\mu$m and $0.5\,\mu$m, respectively. The dust-to-gas mass ratio in the CSM is assumed to be constant and is taken as a free parameter.

Figure 16 illustrates the contribution from CS carbon (Figure 16(a)) and astronomical silicates (Figure 16(b)) for the case of $n_{\rm H,1} = 120$ cm^{-3}, where the ejecta-dust and CS dust components are depicted by the dotted and dashed lines, respectively. The dust-to-gas mass ratios adopted here are 1.6×10^{-4} for carbon and 2.8×10^{-4} for silicate because higher dust-to-gas mass ratios cause excess emission over the observed SED at $\lambda \lesssim 50\,\mu$m. At $t = 330$ yr, the masses of shock-heated CS carbon and silicate grains are $1.4 \times 10^{-3}\,M_\odot$ and $1.8 \times 10^{-3}\,M_\odot$, respectively, and both grain species have typical temperatures of $\simeq$100 K. Thus, we can see that both grain species can only contribute to the SED at $\lambda \lesssim 50\,\mu$m with the peaks around $\lambda = 30\,\mu$m, and cannot compensate the flux densities at $\lambda \geqslant 50\,\mu$m. This means that the observed SED cannot be improved by the contributions from CS grains even if we consider any mixtures of these CS grains and dust-to-gas mass ratios different from those considered here. Therefore, we suppose that the IR emissions from shocked CS grains should not significantly contribute to the IR SED of Cas A and that a small content of CS dust may be due to low condensation efficiency of dust in the mass-loss wind and/or to partial destruction of CS dust by the strong radiation associated with the shock breakout at the explosion (e.g., Blinnikov et al. 1998). We emphasize that the thermal emission from CS dust alone can never reproduce the observations of Cas A for any models considered in this paper.

5.2.3. Contribution from Unshocked Ejecta-dust

As shown in Section 5.2.1, in the case of $n_{\rm H,1} = 120$ cm^{-3}, only $0.008\,M_\odot$ of newly formed dust grains is heated in the shocked gas at $t = 330$ yr, and $0.072\,M_\odot$ of dust grains remains cold without being swept up by the reverse shock (see Table 3). These unshocked dust grains are expected to be heated up by absorbing the X-ray and UV/optical photons generated from the shock-heated plasma and dense knots, and they may radiate their thermal emission with a higher temperature than that ($\sim$20 K) in

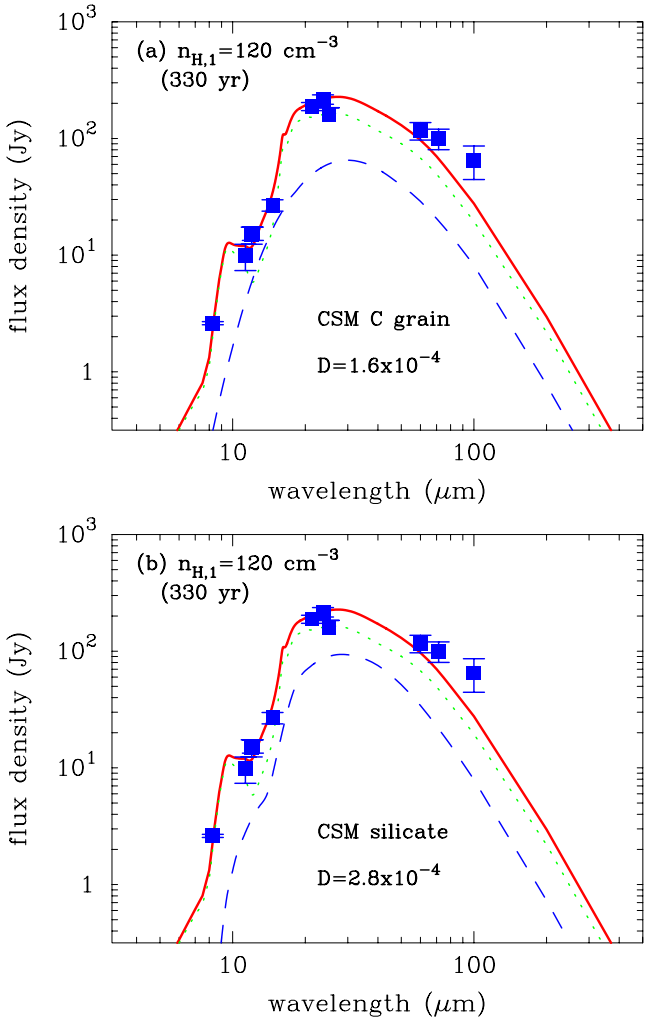

Figure 16. Contributions from (a) CS amorphous carbon and (b) CS astronomical silicate to the IR SED calculated for $n_{H,1} = 120$ cm^{-3}. The dashed and dotted lines denote the thermal emissions from the shocked CS dust and shocked newly formed dust, respectively, and the solid lines represent the total SED. The observation data for Cas A are the same as in Figure 11.

(A color version of this figure is available in the online journal.)

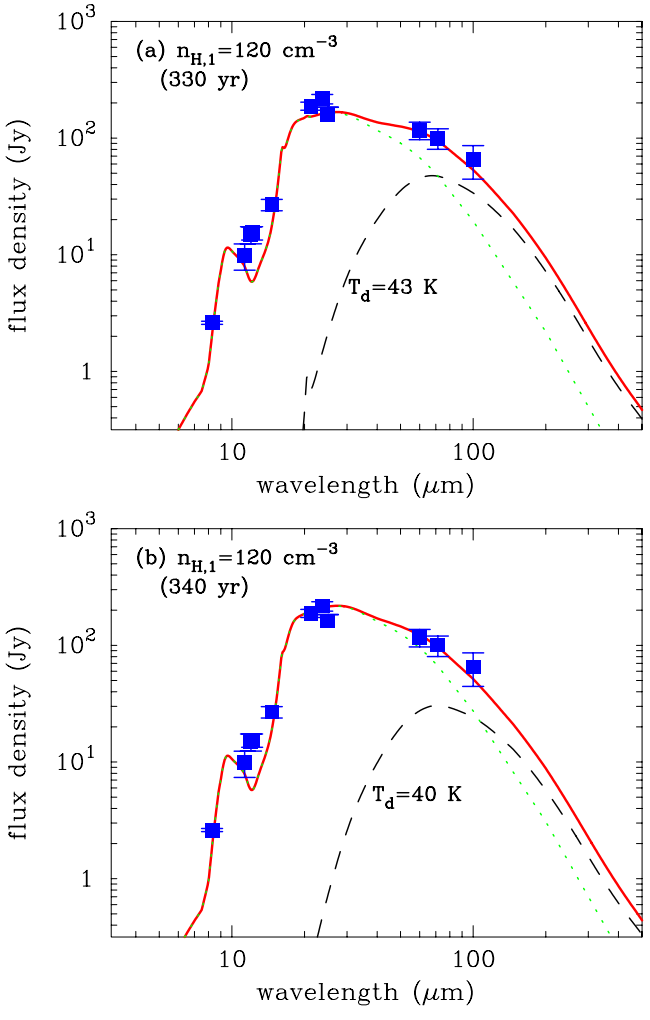

Figure 17. Contributions from the unshocked ejecta-dust to the IR SED calculated for $n_{H,1} = 120$ cm^{-3} at (a) 330 yr and (b) 340 yr. The dashed and dotted lines denote the thermal emissions from the unshocked and shocked newly formed dust, respectively, and the solid lines represent the total SED. The temperature of cold dust is 43 K in (a) and 40 K in (b). The observation data for Cas A are the same as in Figure 11.

(A color version of this figure is available in the online journal.)

the diffuse ISM and contribute to the SED at IR wavelengths. In fact, the presence of cold dust in the unshocked ejecta of Cas A SNR has been suggested from the association of a "featureless dust" component with the Si II emission from the central part of the remnant (Rho et al. 2008). Since the dedicated calculations of radiative transport at X-ray to optical wavelengths is beyond the scope of this paper, we evaluate the contribution of the unshocked dust to the IR SED, assuming the same temperature for all unshocked grains.

Figure 17 shows the contribution from unshocked newly formed dust, together with the contribution of shock-heated warm dust at 330 yr (Figure 17(a)) and 340 yr (Figure 17(b)) for $n_{H,1} = 120$ cm^{-3}. The age of 340 yr is the expected age of Cas A in the case where the forward shock has not been decelerated (Thorstensen et al. 2001; Fesen et al. 2006a). As can be seen from the figures, if the unshocked dust grains are heated up to a temperature around 40 K, their thermal emission can significantly contribute to flux densities at $\lambda \gtrsim 50\,\mu$m and can successfully reproduce the observations of Cas A. Thus, the IR SED observed for Cas A can be naturally explained by the shocked warm component and unshocked cold component of newly formed dust obtained by our calculations. We also note that the calculated IR emission from shocked warm dust at $t = 340$ yr slightly increases from that at $t = 330$ yr, giving a better fit at $\lambda \simeq 20\,\mu$m. This indicates that the IR flux from Cas A can change during a short time interval of $\sim$10 yr.

Finally, the following should be pointed out here. We show that the IR observations of Cas A are successfully reproduced by $0.008\,M_\odot$ shocked dust and $0.072\,M_\odot$ unshocked dust, considering the destruction and heating of newly formed dust in the SNR for $n_{H,1} = 120$ cm^{-3}. Although the derived dust mass in Cas A SNR is superficially large enough to explain a vast amount of dust observed in the host galaxies of high-redshift quasars at $z > 5$, these dust grains would be completely destroyed in 2×10^4 yr and could not be supplied into the ISM, as demonstrated in Section 3.2, if the CSM is more or less spherical. We also should note that if the CSM is not spherical, a portion of the dust grains in the unshocked ejecta could be ejected into the ISM.

6. CONCLUSION

We investigate the formation of dust in the ejecta of a hydrogen-poor SN IIb, adopting the SN model with $E_{kin} = 10^{51}$

erg, $M_{\rm eje} = 2.94\,M_\odot$, and $M_{\rm env} = 0.08\,M_\odot$. Then we explore the evolution of newly formed dust in the hot gas inside the SNR by considering the two sets of density profile for the spherical CSM. Based on the results of dust evolution in SNRs, we also calculate the time evolution of thermal emission from the shocked dust within the SNR and compare the results with the observations of Cas A. The results of our calculations are summarized as follows.

1. In the unmixed ejecta of the SN IIb, various dust species can condense depending on the elemental composition in each layer at 300–700 days after the explosion. The total mass of newly formed dust is as large as $0.167\,M_\odot$, and the composition and mass of dust formed in the SN IIb are similar to those in SNe II-P. However, the mass of the hydrogen envelope of the SN IIb is too small to significantly decelerate the expansion of the He core. Thus, the gas density in the He core is too low for large-sized grains to be produced, and the resulting average radius of dust is smaller than $0.01\,\mu$m. We propose that the size of dust formed in SNe with low-mass envelopes such as SNe IIb as well as the envelope-stripped SNe Ib/Ic is much smaller than that formed in SNe II-P with massive hydrogen envelopes.
2. The evolution of dust within SNRs is strongly affected by the mass of the outer envelope and the gas density in the CSM. A less massive outer envelope and/or a denser CSM lead to the earlier arrival of the reverse shock at the He core, and causes quicker and more efficient destruction of newly formed dust in the denser hot gas. In the Type IIb SNR, as a result of the small size of dust and the early propagation of the reverse shock into the dust-forming region, all newly formed dust grains are destroyed in the shocked gas without being injected into the ISM for the ambient gas density of $n_{\rm H} > 0.1$ cm^{-3}. If the CSM is more or less spherical, our results imply that low-mass envelope SNe do not play a major role in the dust enrichment in the ISM.
3. The time evolution of IR SEDs by thermal emission from shocked dust in SNRs well reflects the evolution of dust through erosion by sputtering and stochastic heating. The destruction and heating processes of dust in the hot gas are heavily affected by the ambient gas density that affects the passage of the reverse shock into the ejecta. Thus, the comparison of theoretically modeled SEDs and observed IR SEDs can be used to diagnose the size and mass of dust in SNRs and the density structure surrounding the SNe. These in turn provide us with some hints on the formation process of dust in the ejecta and the mass-loss activity of the progenitor stars during late evolution.
4. The IR SED observed for Cas A can be reasonably reproduced by the shocked warm dust with $M_d = 0.008\,M_\odot$ and unshocked cold dust with $M_d = 0.072\,M_\odot$, both of which were newly formed in the ejecta. The CSM density required to reproduce the observed SED corresponds to the steady stellar wind of a supergiant with a mass-loss rate of $8 \times 10^{-5}\,M_\odot$ yr^{-1}. This mass-loss rate is consistent with those estimated for the progenitors of SN 1993J and Cas A within a factor of 2–4. It should be emphasized that these conclusions are the natural outcomes derived by the self-consistent treatments of formation, destruction, and heating of dust given in this study.

The result of the dust formation calculation shows that the total mass of dust formed in the ejecta is $0.167\,M_\odot$, which is much larger than the mass estimate of dust deduced from the observations of nearby dust-forming SNe. From the comparison of calculated SEDs with the observed SED, we predict that in Cas A SNR about half the newly formed dust grains have already been swept up by the reverse shock and most of them had been destroyed, while the other half of newly formed grains have not yet been swept up by the reverse shock. The mass of this unshocked dust ($0.072\,M_\odot$) is in good agreement with the upper mass limit of cold dust ($0.2\,M_\odot$) in Cas A estimated by Krause et al. (2004). On the other hand, our calculation demonstrates that all dust grains formed in Cas A might be completely destroyed later on and might not be injected into the ISM, if the CSM was more or less spherical (see below). Thus, the SN IIb that formed Cas A might not be representative of SNe as major sources of interstellar dust, but Cas A could remain as a unique and ideal object for investigating formation and evolution processes of dust in SNe.

We should bear in mind that all calculations here are performed for the spherically symmetric forward and reverse shocks propagating into the homogeneous CSM and stratified ejecta, respectively. In the binary scenario for SNe IIb (Nomoto et al. 1995, 1996), the formation of aspherical CSM is predicted to be as follows. The close binary consists of a massive SN IIb progenitor and a small-mass companion star. In the common envelope phase, the companion star spirals into the envelope of the SN IIb progenitor, which causes extensive mass loss from the H-rich envelope of the progenitor in the direction of the equatorial plane. The resultant CSM might have a ring-like structure as seen in SN 1987A, a torus, or a thick disk. In reality, the CSM around SN 1993J is considered to be more like a torus shape (e.g., Fransson et al. 2005). Then since the ejecta of polar direction cannot strongly interact with the CSM (e.g., Maeda et al. 2002), the ejecta of SN 1993J can be composed of the reverse-shocked ejecta and the unshocked ejecta. Thus, if the CSM is spherical, dust can be totally destroyed. If the CSM is non-spherical like SN 1993J, unshocked dust can be partially ejected.

In addition, IR and X-ray observations of Cas A have shown that the ejecta of Cas A are very clumpy and asymmetric (Willingale et al. 2002; Ennis et al. 2006; Smith et al. 2009) with the inverted compositions as represented by Fe-rich materials overtaking the outer layer (e.g., Hughes et al. 2000). This indicates that some dust species may encounter the reverse shock at different times and different gas densities than suggested in this paper. Furthermore, if newly formed grains would reside in dense clumps, it might be possible that a part of them could survive the destruction and be injected into the ISM. Although the mass of shocked and visible material is believed to roughly account for all the mass ejected in the explosion, the IR spectral mapping observations of the entire region of Cas A SNR suggest the presence of unshocked ejecta materials in the central region of the remnant (Rho et al. 2008; Smith et al. 2009). However, it has been difficult to estimate how much dust there is in the unshocked region from the observations covering the wavelengths of $\lambda \leqslant 70\,\mu$m, as pointed out by Rho et al. (2008). Since the mass of dust in Cas A is likely to be dominated by the unshocked low-temperature dust, comprehensive far-IR observations at $\lambda \gtrsim 50\,\mu$m are necessary to reveal the mass of dust formed in the Cas A SN.[6] Unfortunately, Cas A suffers from

[6] After this paper was submitted, an article by Sibthorpe et al. (2009) appeared on astro-ph reporting the presence of a cool emission component peaked near the center of Cas A in the 90 μm image obtained by the *AKARI*. They suggest that this emission comes from unshocked newly formed dust in Cas A and estimate its mass to be 0.03–0.06 $M_\odot$.

contamination from interstellar dust in the foreground molecular clouds, but the *Herschel* will be able to give more critical clues on the mass of cold dust in Cas A.

The authors are grateful to the anonymous referee for critical comments that were useful for improving the manuscript. T.N. and T.K. acknowledge Th. Henning and all members for the kind hospitality during their stay at MPIA. This research has been supported in part by World Premier International Research Center Initiative (WPI Initiative), MEXT, Japan, and by the Grant-in-Aid for Scientific Research of the Japan Society for the Promotion of Science (18104003, 19740094, 20340038, 20540226, 20540227, 20840007, 21840055) and MEXT (19047004, 20040004).

REFERENCES

Arendt, R. G., Dwek, E., & Moseley, S. H. 1999, ApJ, 521, 234
Begemann, B., Dorschner, J., Henning, Th., Mutschke, H., Gütler, J., Kömpe, C., & Nass, R. 1997, ApJ, 476, 199
Bianchi, S., & Schneider, R. 2007, MNRAS, 378, 973
Blinnikov, S. I., Eastman, R., Bartunov, O. S., Popolitov, V. A., & Woosley, S. E. 1998, ApJ, 496, 454
Boissier, S., & Prantzos, N. 2009, A&A, 503, 137
Borkowski, K. J., Szymkowiak, A. E., Blondim, J. M., & Sarazin, C. L. 1996, ApJ, 466, 866
Chevalier, R. A., & Oishi, J. 2003, ApJ, 593, L23
Deneault, E. A.-N., Clayton, D. D., & Heger, A. 2003, ApJ, 594, 312
Dorschner, J., Begemann, B., Henning, Th., Jäger, C., & Mutschke, H. 1995, A&A, 300, 503
Douvion, T., Lagage, P. O., & Pantin, E. 2001, A&A, 369, 589
Draine, B. T., & Lee, H. M. 1984, ApJ, 285, 89
Dunne, L., Eales, S., Ivison, R., Morgan, H., & Edmunds, M. 2003, Nature, 424, 285
Dunne, L., et al. 2009, MNRAS, 394, 1307
Dwek, E. 1986, ApJ, 302, 363
Dwek, E. 1987, ApJ, 322, 812
Dwek, E. 2004, ApJ, 607, 848
Dwek, E., Dinerstein, H. L., Gillett, F. C., Hauser, M. G., & Rice, W. L. 1987, ApJ, 315, 571
Dwek, E., Galliano, F., & Jones, A. P. 2007, ApJ, 662, 927
Edoh, O. 1983, PhD thesis, Univ. of Arizona
Ennis, J. A., Rudnick, L., Reach, W. T., Smith, J. D., Rho, J., DeLaney, T., Gomez, H., & Kozasa, T. 2006, ApJ, 652, 376
Ercolano, B., Barlow, M. J., & Sugerman, B. E. K. 2007, MNRAS, 375, 753
Favata, F., et al. 1997, A&A, 324, L49
Fesen, R. A. 2001, ApJS, 133, 161
Fesen, R. A., & Becker, R. H. 1991, ApJ, 371, 621
Fesen, R. A., et al. 2006a, ApJ, 636, 859
Fesen, R. A., et al. 2006b, ApJ, 645, 283
Fransson, C., Lundqvist, P., & Chevalier, R. A. 1996, ApJ, 461, 993
Fransson, C., et al. 2005, ApJ, 622, 991
Gotthelf, E. V., Koralesky, B., Rudnick, L., Jones, T. W., Hwang, U., & Petre, R. 2001, ApJ, 552, L39
Hachisu, I., Matsuda, T., Nomoto, K., & Shigeyama, T. 1990, ApJ, 358, L57
Hachisu, I., Matsuda, T., Nomoto, K., & Shigeyama, T. 1992, ApJ, 390, 230
Hasegawa, H., & Kozasa, T. 1988, Prog. Theor. Phys. Suppl., 96, 107
Hines, et al. 2004, ApJS, 154, 290
Hirashita, H., Nozawa, T., Takeuchi, T. T., & Kozasa, T. 2008, MNRAS, 384, 1725
Hughes, J. P., Rakowski, C. E., Burrows, D. N., & Slane, P. O. 2000, ApJ, 528, L109
Iskef, H., Cunningham, J. W., & Watt, D. E. 1983, Phys. Med. Biol., 28, 535
Iwamoto, K., Young, T., Nakasato, N., Shigeyama, T., Nomoto, K., Hachisu, I., & Saio, H. 1997, ApJ, 477, 865
Kotak, R., et al. 2009, ApJ, 704, 306
Kozasa, T., & Hasegawa, H. 1987, Prog. Theor. Phys., 77, 1402
Kozasa, T., Hasegawa, H., & Nomoto, K. 1989, ApJ, 344, 325
Kozasa, T., Hasegawa, H., & Nomoto, K. 1991, A&A, 249, 474
Kozasa, T., Nozawa, T., Tominaga, N., Umeda, H., Maeda, K., & Nomoto, K. 2009, in ASP Conf. Ser., Cosmic Dust: Near and Far, ed. Th. Henning, E. Grüm, & J. Steinacker (San Francisco, CA: ASP), in press (arXiv: 0903.0217)
Krause, O., Birkmann, S. M., Rieke, G. H., Lemke, D., Klaas, U., Hines, D. C., & Gordon, K. D. 2004, Nature, 432, 596
Krause, O., Birkmann, S. M., Usuda, T., Hattori, T., Goto, M., Rieke, G. H., & Misselt, K. A. 2008, Science, 320, 1195
Lagage, P. O., Claret, A., Ballet, J., Boulanger, F., Césarsky, C. J., Césarsky, D., Fransson, C., & Pollock, A. 1996, A&A, 315, L273
Laming, J. M., & Hwang, U. 2003, ApJ, 597, 347
Maeda, K., Nomoto, K., Nakasato, N., & Suzuki, T. 2002, in ASP Conf. Ser. 271, Neutron Stars in Supernova Remnants, ed. P. O. Slane & B. M. Gaensler (San Francisco, CA: ASP), 379
Maiolino, R., et al. 2006, Mem. Soc. Astron. Ital., 77, 643
Mathis, J. S., Rumpl, W., & Nordsieck, K. H. 1977, ApJ, 217, 425
Mattila, S., et al. 2008, MNRAS, 389, 141
Meikle, W. P. S., et al. 2007, ApJ, 665, 608
Morgan, H. L., & Edmunds, M. G. 2003, MNRAS, 343, 427
Nomoto, K., Iwamoto, K., & Suzuki, T. 1995, Phys. Rep., 256, 173
Nomoto, K., Iwamoto, K., Suzuki, T., Pols, O. R., Yamaoka, H., Hashimoto, M., Hoeflich, P., & van den Heuvel, E. P. J. 1996, in IAU Symp. 165, Compact Stars in Binaries, ed. J. van Paradijs, E. P. J. van den Heuvel, & E. Kuulkers (Dordrecht: Kluwer), 119
Nomoto, K., Suzuki, T., Shigeyama, T., Kumagai, S., Yamaoka, H., & Saio, H. 1993, Nature, 364, 507
Nozawa, T., Kozasa, T., & Habe, A. 2006, ApJ, 648, 435
Nozawa, T., Kozasa, T., Habe, A., Dwek, E., Umeda, H., Tominaga, N., Maeda, K., & Nomoto, K. 2007, ApJ, 666, 955
Nozawa, T., Kozasa, T., Umeda, H., Maeda, K., & Nomoto, K. 2003, ApJ, 598, 785
Nozawa, T., et al. 2008, ApJ, 684, 1343
Philipp, H. R. 1985, in Handbook of Optical Constants of Solids, ed. E. D. Palik (San Diego, CA: Academic), 719
Piller, H. 1985, in Handbook of Optical Constants of Solids, ed. E. D. Palik (San Diego, CA: Academic), 571
Podsiadlowski, Ph., Hsu, J. J. L., Joss, P. C., & Ross, R. R. 1993, Nature, 364, 509
Prieto, J. L., Stanek, K. Z., & Beacom, J. F. 2008, ApJ, 673, 999
Reed, J. E., Hester, J., Fabian, A. C., & Winkler, P. F. 1995, ApJ, 440, 706
Rho, J., et al. 2008, ApJ, 673, 271
Roessler, D. M., & Huffman, D. R. 1991, in Handbook of Optical Constants of Solids II, ed. E. D. Palik (San Diego, CA: Academic), 919
Sakon, I., et al. 2009, ApJ, 692, 546
Semenov, D., Henning, Th., Helling, Ch., Ilgner, M., & Sedlmayr, E. 2003, A&A, 410, 611
Shigeyama, T., Suzuki, T., Kumagai, S., Nomoto, K., Saio, H., & Yamaoka, H. 1994, ApJ, 420, 341
Sibthorpe, B., et al. 2009, ApJ, submitted (arXiv:0910.1094)
Smartt, S. J., Eldridge, J. J., Crockett, R. M., & Maund, J. R. 2009, MNRAS, 395, 1409
Smith, N., Foley, R. J., & Filippenko, A. V. 2008, ApJ, 680, 568
Smith, J. D. T., Rudnick, L., DeLaney, T., Rho, J., Gomez, H., Kozasa, T., Reach, W. T., & Isensee, K. 2009, ApJ, 693, 713
Sugerman, B. E. K., et al. 2006, Science, 313, 196
Suzuki, T., & Nomoto, K. 1995, ApJ, 455, 658
Tabata, T., Ito, R., & Okabe, S. 1972, Nucl. Instrum. Methods, 103, 85
Takeuchi, T. T., Ishii, T. T., Nozawa, T., Kozasa, T., & Hirashita, H. 2005, MNRAS, 362, 592
Thorstensen, J. R., Fesen, R. A., & van den Bergh, S. 2001, AJ, 122, 297
Todini, P., & Ferrara, A. 2001, MNRAS, 325, 726
Tominaga, N. 2009, ApJ, 690, 526
Tominaga, N., et al. 2008, ApJ, 687, 1208
Toon, O. B., Pollack, J. B., & Khare, B. N. 1976, J. Geophys. Res., 81, 5733
Umeda, H., & Nomoto, K. 2002, ApJ, 565, 385
Valiante, R., Schneider, R., Bianchi, S., & Andersen, A. C. 2009, MNRAS, 397, 1661
Vink, J., Kaastra, J. S., & Bleeker, J. A. M. 1996, A&A, 307, L41
Willingale, R., Bleeker, J. A. M., van der Heyden, K. J., & Kaastra, J. S. 2003, A&A, 398, 1021
Willingale, R., Bleeker, J. A. M., van der Heyden, K. J., Kaastra, J. S., & Vink, J. 2002, A&A, 381, 1039
Wilson, T. L., & Batrla, W. 2005, A&A, 430, 561
Young, P. A., et al. 2006, ApJ, 640, 891